Journal of Alloys and Compounds 916 (2022) 165465

Contents lists available at ScienceDirect

Journal of Alloys and Compounds

journal homepage: www.elsevier.com/locate/jalcom

Recrystallization mechanisms and associated microstructure evolution during billet conversion of a gamma-gamma′ nickel based superalloy

A. Coyne-Grell[a,*], J. Blaizot[b], S. Rahimi[a], I. Violatos[a], S. Nouveau[b], C. Dumont[b], A. Nicolaÿ[c], N. Bozzolo[c]

[a] Advanced Forming Research Centre (AFRC), University of Strathclyde, 85 Inchinnan Drive, Inchinnan PA4 9LJ, United Kingdom
[b] Aubert & Duval, Site des Ancizes, BP1, 63770 les Ancizes Cedex, France
[c] MINES ParisTech, PSL – Research University, CEMEF – Centre de mise en forme des materiaux, Sophia – Antipolis, France

ARTICLE INFO

Article history:
Received 10 February 2022
Received in revised form 12 May 2022
Accepted 14 May 2022
Available online 18 May 2022

Keywords:
Recrystallization
Microstructure
Precipitation
Scanning electron microscopy
Metals and alloys

ABSTRACT

A partially recrystallized sample of the Ni-based superalloy AD730 was taken from an intermediate stage of the ingot to billet conversion process and isothermally forged in a single stroke compression test at a sub-solvus temperature (1080 °C). The as-received material had a heterogeneous microstructure, containing a mixture of coarse and much finer recrystallized grains as well as unrecrystallized ones, and also heterogeneous γ′ precipitation. The recrystallization mechanisms occurring dynamically in the different grain populations were investigated via electron backscatter diffraction (EBSD). It was found that local microstructure could affect the operative recrystallization mechanism, with different mechanisms seen in the deformed and recrystallized regions, owing to their different precipitate distributions. Within a single deformed grain, three apparently distinct dynamic recrystallization (DRX) mechanisms were identified. The interaction of recrystallization with precipitates plays a central role in DRX. In certain cases precipitates may stimulate discontinuous DRX by providing recrystallization nuclei, alternatively they may impede and limit the growth of recrystallized grains, or in other cases still they promote continuous recrystallization.

1. Introduction

AD730 is a Ni-based superalloy intended for use in jet engine turbine discs which has been developed relatively recently [1]. This alloy is processed through the cast and wrought route, and offers good high temperature properties as compared with other cast and wrought Ni-based superalloys (e.g., IN718 and 718 plus), as well as being relatively low cost due to its limited content of expensive alloying additions such as cobalt and niobium. As such, the alloy sits between traditional cast and wrought alloys and powder metallurgy alloys in cost - performance space.

The microstructure of AD730 comprises a γ matrix with a disordered FCC crystal structure and γ′ precipitates with an ordered $L1_2$ crystal structure [2]. The solvus temperature for the γ′ precipitates in AD730 has been determined to be ≈ 1110 °C [3]. The coherent, ordered precipitates provide the alloy's high temperature strength through the order hardening mechanism.

The microstructural control of Ni-based superalloys through thermo-mechanical processing (TMP) has long been of academic and industrial interest. Microstructural characteristics are tailored via TMP to ensure the required mechanical properties are achieved. Recrystallization (RX) is one of the important microstructural evolutionary mechanisms that occurs during TMP through which the grain size distribution of a material can be controlled. Recrystallization may occur either during hot deformation (i.e., forging), known as dynamic recrystallization (DRX), or after deformation while the material is cooling from the forging temperature, known as post-dynamic recrystallization (PDRX).

Due to their importance in controlling microstructure, recrystallization mechanisms have been studied extensively in Ni-based superalloys at both γ′ sub-solvus and super-solvus temperatures, and the influence of TMP parameters on recrystallization has been well investigated [4–21]. However, only a small minority of these studies [4,5], consider non-homogenous starting microstructures. This is not representative of the intermediate stages of the ingot to billet conversion process, where billets are "partially forged". Here, a non-homogenous microstructure, consisting of a mixture of large unrecrystallized and small recrystallized grains is typical. Indeed, achieving a fully recrystallized microstructure in a

* Corresponding author.
E-mail address: angus.coyne@strath.ac.uk (A. Coyne-Grell).

https://doi.org/10.1016/j.jallcom.2022.165465
0925-8388/

Table 1
Nominal chemical composition of the AD730 alloy.

Element	Ni	Fe	Cr	Co	Mo	W	Al	Ti	Nb	C	B	Zr
Weight %	Bal.	4.0	15.7	8.5	3.1	2.7	2.25	3.4	1.1	0.02	0.01	0.03

billet during this conversion process is not so straightforward, and large unrecrystallized grains may survive after the ingot to billet conversion [22,23]. Industrial scale ingot to billet conversion processes comprise multiple forging and heating steps, and only towards the end of this process will a homogenous microstructure be achieved. Despite this, there are limited studies which consider dynamic recrystallization in samples from an intermediate stage of the ingot to billet conversion process, where the microstructures are far more heterogeneous (e.g., [5]). The vast majority of the reported studies are on "fully forged" billet materials, and not on "partially forged" materials from the intermediate stages of ingot to billet conversion.

During ingot to billet conversion of Ni-based superalloys, where a mixture of both recrystallized and unrecrystallized grains are present, the unrecrystallized grains appear to contain a finer and denser distribution of the γ' precipitation than the recrystallized grains. This has been seen during forging of René65 [23], Udimet720-Li, and AD730 [24]. Seret et al. observed a finer and denser distribution of γ' in unrecrystallized grains of AD730 after cooling a partially recrystallized sample from super-solvus temperatures [25]. It was argued that the elastic strain field generated by the dislocations in the unrecrystallized grains locally lowered the energy barrier for the nucleation of precipitates, providing a high number of kinetically favoured nucleation sites.

Additionally, large recrystallized grains, which grow by consuming a neighbouring deformed grain, have been observed to form in the γ-γ' superalloys AD730, René 65 and PER72 during static recrystallization treatment by Vernier et al. [26,27]. These large, statically recrystallized grains shared a < 111 > axis with a neighbouring deformed grain, and this permitted them to grow and overcome the precipitation in the neighbouring deformed grain via a particular mechanism. This mechanism involves the precipitates in the deformed grain being dissolved and reprecipitated at the moving interface between the growing recrystallised and the deformed grain [26]. This results in reprecipitation of the precipitates such that they share a common < 111 > axis with both the growing recrystallised and the deformed grain. It was suggested that this allowed the precipitates to minimise their interfacial energy with respect to both the deformed and recrystallized grains when forming at the interface between the two [26]. These precipitates also develop < 111 > facets, so overall this mechanism results in large statically recrystallised grains which contain γ' precipitates with rectangular shapes (as seen in 2D sections), which are either close to coherent with their host grain (called C type precipitates), or close to twin related to it (called T type precipitates).

In γ - γ' alloys in particular, the heterogeneous microstructure is expected to have a strong influence on recrystallization behaviour, as different distributions of the γ' precipitates interact differently with recrystallization. The progression of recrystallization requires the recrystallization front to overcome the precipitates encountered. This can be achieved by the front dissolving precipitates, which are then reprecipitated behind it (i.e., in the recrystallized grains) [28]. This has been observed in AD730 [25]. However, in some cases the moving recrystallization front is unable to overcome the encountered precipitates, which hinders recrystallization. This was seen in unrecrystallized grains with a relatively fine and dense precipitation distribution in AD730 [29]. Near γ' solvus heat treatments, which promote a more coarse and sparse distribution, can thus be useful to promote full recrystallization, and this has been demonstrated in Udimet 720Li [30].

This work aims to characterise the recrystallization mechanisms happening in the Ni-based superalloy AD730 during sub-solvus forging of a sample taken from an intermediate stage of the ingot to billet conversion process. At this intermediate stage the sample possesses a rather heterogeneous microstructure. The focus is on describing these mechanisms based on measurable features developed during recrystallization, such as the orientation, location, size, intragranular misorientations, and interactions with γ' precipitates of the recrystallized and unrecrystallized grains involved. Since different recrystallization mechanisms produce different microstructural features, different mechanisms can be identified and characterised based on the microstructures they produce. This is done under a single set of TMP parameters, so that different recrystallization processes are attributable primarily to different local microstructural conditions (i.e., grain size, precipitate distribution and stored energy), rather than differences in the nominal conditions.

2. Material and methods

2.1. Material and compression testing

AD730 material from an intermediate stage of the ingot to billet conversion was supplied by Aubert & Duval™ as the starting material for these investigations. This material had been triple melted (i.e., vacuum induction melted, electro-slag re-melted, and vacuum arc re-melted) and had undergone super- and sub-solvus forging and upsetting steps, as well as a static recrystallization treatment. This material will henceforth be referred to as "partially forged". The material was in the form of a square bar, with a cross section of 20 × 20 mm^2, and a length of approximately 55 mm cut parallel to a radial direction of the "partially forged" billet. The nominal composition of this material is given in Table 1. A cylindrical compression sample with φ 10 mm × 15 mm dimensions was cut from the as-received material, such that the cylindrical axis of the sample was parallel to a radial direction of the "partially forged" billet.

Compression testing was done in an MTS 250 machine equipped with a furnace. The sample was placed in the furnace at 1080 °C and soaked for 5 min to allow temperature homogenisation. The sample was then deformed in compression to a 50% reduction in height, corresponding to a macroscopic true strain (ε_m) of 0.7, under a nominal strain rate of 0.1 s^{-1} ($\dot{\varepsilon}_m$). Graphite foils were placed at the tool/sample interfaces for lubrication. As quickly as possible after deformation, the furnace was lifted out and the sample was removed and quenched in water. Water quenching was recorded on video, and in practice the delay between the end of deformation and the sample being quenched was 3.0 s. A schematic plot of the thermo-mechanical procedure for the compression test is shown in Fig. 1(a).

2.2. Finite element analysis

A 2D axisymmetric finite element (FE) simulation of the compression test, including the initial heating and soaking stages, was performed using the DEFORM software to predict the strain distribution at different locations along the sample. Material data for AD730 in the temperature range 300–1200 °C was supplied by Aubert & Duval. A heat transfer coefficient of 11 mW/m^2K and a friction coefficient of 0.3 between the dies and the sample were implemented, as per the software's suggested values for lubricated hot forging. A Taylor-Quinny factor of 0.9 was used, which is a good

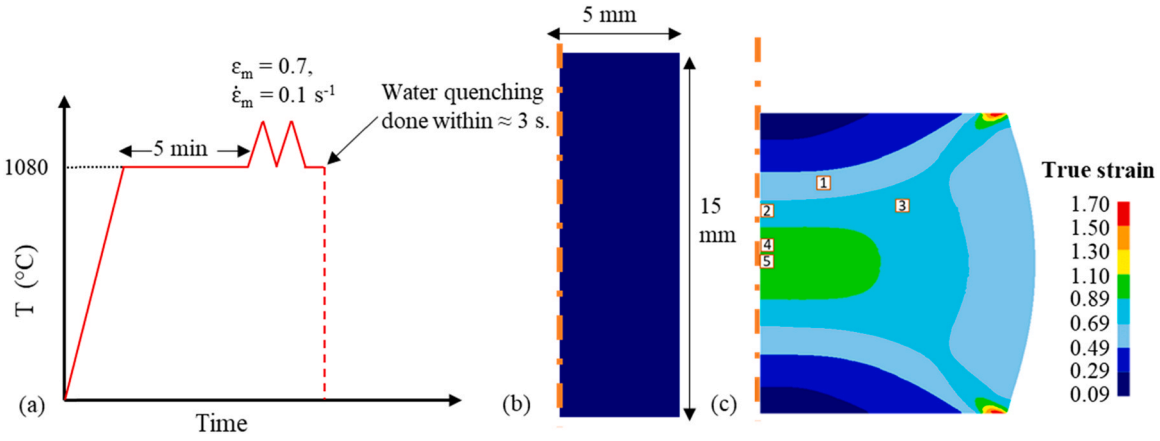

Fig. 1. (a) Schematic overview of the compression trial in this study, (b) a sketch of the sample geometry prior to compression with all dimensions, and (c) the strain distribution after compression predicted by the FE simulation, with the regions from which the EBSD data were collected highlighted and numbered.

approximation of the fraction of mechanical work converted into heat during deformation [31]. The workpiece was meshed into 5102 elements. The upper die's movement speed during the compression test was recorded, and this was used as an input for the FE simulation.

The sample dimensions predicted by the model were compared with the actual dimensions of the deformed cylinder after compression. The model was set up to match the height of the deformed cylinder (7.83 mm), and it predicted a maximum diameter of 14.54 mm, which was within 3% of the measured diameter of 14.13 mm. This validates the chosen values of heat transfer coefficient and friction coefficient, and suggests that the strain distribution is reasonably accurate.

2.3. Microstructure characterisations

The deformed sample was sectioned along the cylindrical axis, mounted in conductive Bakelite and ground and polished to a mirror finished condition, then subjected to a final vibratory polishing for 16 h using 0.02 µm colloidal silica suspension. Backscattered electron (BSE) images and electron backscatter diffraction (EBSD) patterns were acquired using an FEI Quanta 250 field emission gun scanning electron microscope (FEG-SEM) interfaced with a Nordlys EBSD detector and the Channel 5 HKL Flameco software, and a Tescan FERA3 FEG SEM equipped with an Oxford C-Nano detector and the Oxford Aztec 4.1 software. To gain a representative large area overview of the microstructure, maps with an area of approximately 1.24 mm^2 were taken using a step size in the range 2.5–4 µm. In these low magnification maps, at least 80% of the points were indexed in all cases. For more detailed analyses, five smaller EBSD maps were acquired with a smaller step size. The locations of these regions are indicated in Fig. 1(c), and their respective step size and indexing rate are provided in Table 2.

Immediately before and after EBSD scans, forward scattered electron (FSE) images were also captured from the same area using a forward-scattered electron detector (FSD) attached to the EBSD camera. Since these FSE images were captured under identical conditions to the EBSD scans, data from the two can be compared and overlaid (e.g., grain boundaries from the EBSD data overlaid onto the FSE image). This is advantageous in such a γ/γ′ alloy, as these two phases cannot be easily discriminated using EBSD. The two display very similar EBSD patterns [32], and even large (multi-micrometric) primary precipitates can be coherent with their host γ grain in more than 50% of cases [33]. As such, methods based on chemical composition are best suited to distinguish γ′ precipitates from the γ matrix [34].

Table 2
Map properties for five regions investigated with EBSD.

Region number	Local strain	Map area/µm^2	Step size/µm	Indexing rate/%
1	0.53	231.6 × 202.4	0.20	91.0
2	0.72	148.2 × 111.1	0.20	98.5
3	0.76	122.3 × 107.0	0.15	94.0
4	1.00	98.6 × 74.0	0.20	98.5
5	1.04	86.5 × 45.5	0.50	96.2

The EBSD data were analysed using the MTEX toolbox [35] developed in MATLAB. High angle grain boundaries (HAGBs) were defined according to a misorientation angle of at least 10°, and twin boundaries were defined as those with a 60° < 111 > misorientation, allowing an 8.66° tolerance, following the Brandon criterion [36]. Low angle grain boundaries (LAGBs) were defined as boundaries with misorientations between 3° and 5°, and medium angle grain boundaries (MAGBs) were defined as boundaries with misorientation angles between 5° and 10°. Inverse pole figure (IPF) maps were plotted with respect to the compression direction (CD), unless otherwise stated. The colour key used (defined in the standard triangle in Fig. 2(c)) is the same for all figures. Grain boundaries were plotted as black lines, and twin boundaries as red lines. Where EBSD and FSE images were overlaid, the grain boundaries were drawn as blue lines on the FSE image to enhance their contrast. Local misorientations were investigated using the kernel average misorientation (KAM) parameter. KAM is calculated at every EBSD measurement point as the average misorientation angle (in degrees) between the given measurement point and its neighbours. In this case only first order neighbours were considered. The definition for KAM at pixel i, based on its n nearest neighbours (j), is given in Eq. (1).

$$KAM_i = \frac{1}{n}\sum_{j=1}^{n}\theta_{ij} \tag{1}$$

To analyse the distribution of γ′ precipitates, FSE or BSE images were segmented using the Autocontext workflow of ilastik, an image analysis software [37]. The segmented images were then analysed further using ImageJ to obtain statistics relating to precipitate size distribution and area fraction [38].

The 3D shape of precipitates was analysed using FIB-SEM nanotomography. A plasma technology ion column was used inside a Tescan FERA3 FEG SEM equipped with a Xe^+ Plasma-FIB column. A region of interest was selected and 0.1 µm thick slices were consecutively milled away, and a BSE image was collected in between each slice. FIB slicing was done using an accelerating voltage of 30 kV

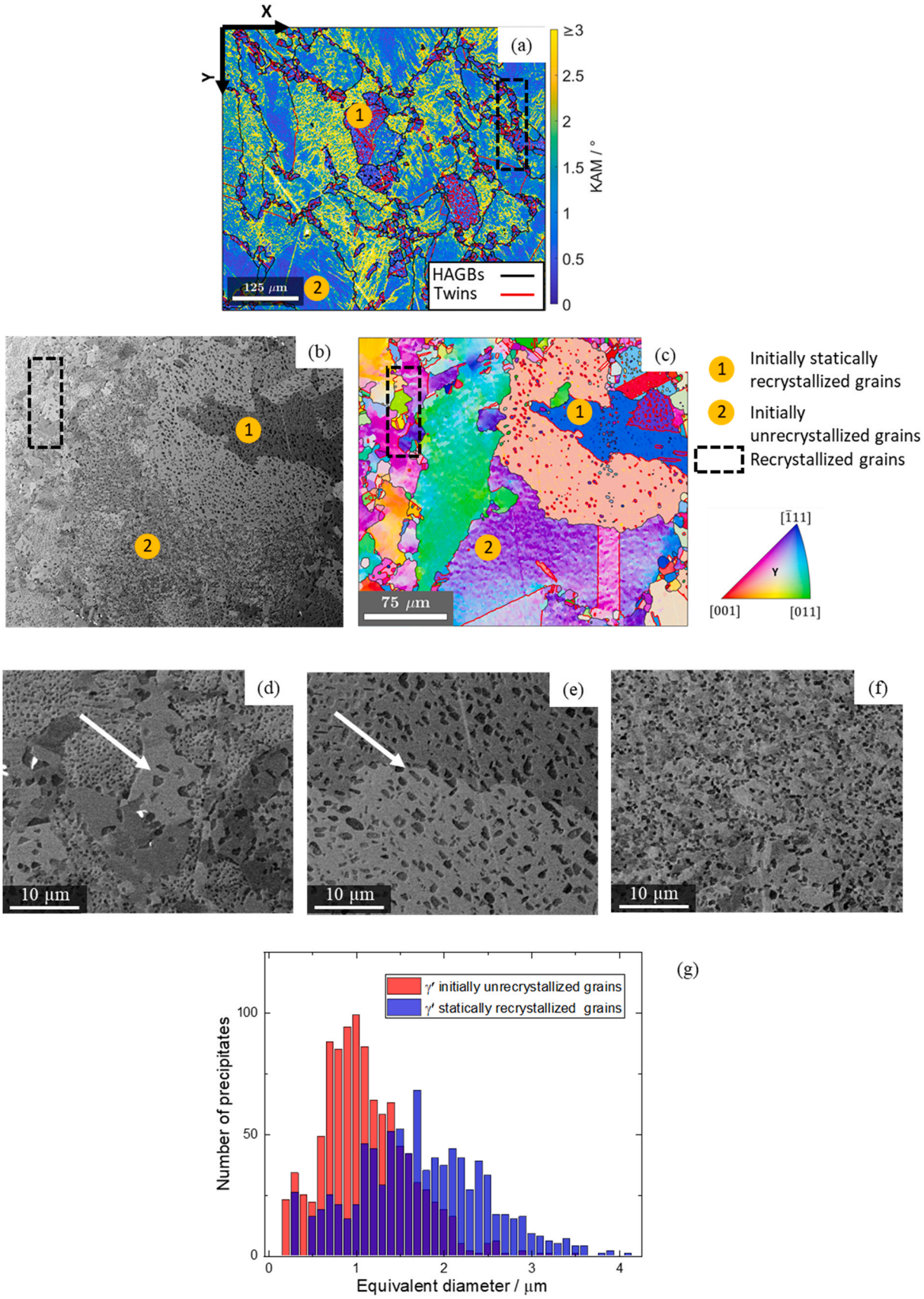

Fig. 2. Microstructure of the as-received AD730 material. (a) A KAM map (values limited to 3°) with three distinct populations of grain highlighted, (b) a BSE micrograph, and (c) its corresponding IPF map colourised with respect to the Y direction. (d), (e), (f) Magnified micrographs of three selected areas highlighted in (b) showing the three distinct precipitation states in recrystallized, initially statically recrystallized and initially unrecrystallized grains, respectively. (g) Histograms of precipitate size distribution in the initially statically recrystallized and the initially unrecrystallized grains.

Table 3
Size and density of the precipitates in the three grain populations in the as-received sample. Values given are in the format of mean ± standard deviation.

Grain type	Equivalent diameter (μm)	Area density (μm^{-2})	Precipitates counted	Precipitate area fraction (%)	Maximum Feret diameter (μm)
Initially statically recrystallized	1.8 ± 0.7	0.074	882	21.7	2.6 ± 1.2
Initially unrecrystallized	1.2 ± 0.5	0.167	1016	20.8	–
Recrystallized	2.2 ± 0.6	–	100	–	–

and a beam current of 30 nA. The resulting stack of 2D images was reconstructed into a 3D image and segmented to separate out γ′ precipitates from the γ matrix. A volume of 35.9 μm × 10.0 μm × 14.9 μm was analysed. The MorphoLib library in ImageJ was used for image processing and analysis [39].

3. Results

3.1. The as-received material and an overview of the effect of strain on microstructure evolution

The microstructure of the "partially forged" as-received material is shown in Fig. 2. The KAM map (Fig. 2(a)) shows that the microstructure was partially recrystallized, and possessed a wide spread of grain sizes. Here the KAM scale has been limited to 3°, and the KAM map can be used to qualitatively distinguish between recrystallized and unrecrystallized grains. A BSE image of a smaller area in the as-received sample is shown in Fig. 2(b), along with its associated IPF map in Fig. 2(c). Fig. 2(d)–(f) are BSE micrographs depicting γ' precipitates with different sizes and morphologies taken from different regions of Fig. 2(b). From these observations, three different grain populations can be identified as the following:

(i) Large grains (equivalent diameters ≈ 28.4 μm) which have low internal KAM values (only a few points > 1.5°). The low KAM values indicate low levels of internal misorientation, as such these grains can be classed as statically recrystallized. They contain γ′ precipitates which display a rectangular morphology in the 2D cross-sections revealed in the micrographs, and have either a close to twin or close to coherent crystallographic orientation relationship with their host γ grains. Here, close to coherent means that the precipitates' orientations are sufficiently close to those of their host grains that they cannot be distinguished based on EBSD data, implying a misorientation angle ≤ 0.5°. Note this is somewhat different from the strict crystallographic definition of the term coherent. Vernier et al. have described the formation of such grains during the static recrystallization of AD730, René 65 and PER72 [26]. These will thus be referred to as "initially statically recrystallized grains" hereafter.

(ii) Large grains (equivalent diameters ≈ 61.0 μm) with high internal KAM values (many points > 1.5°). These are unrecrystallized grains, which are generally larger than the initially statically recrystallized grains and show higher KAM values, indicating higher internal misorientation, and stored energy manifested in

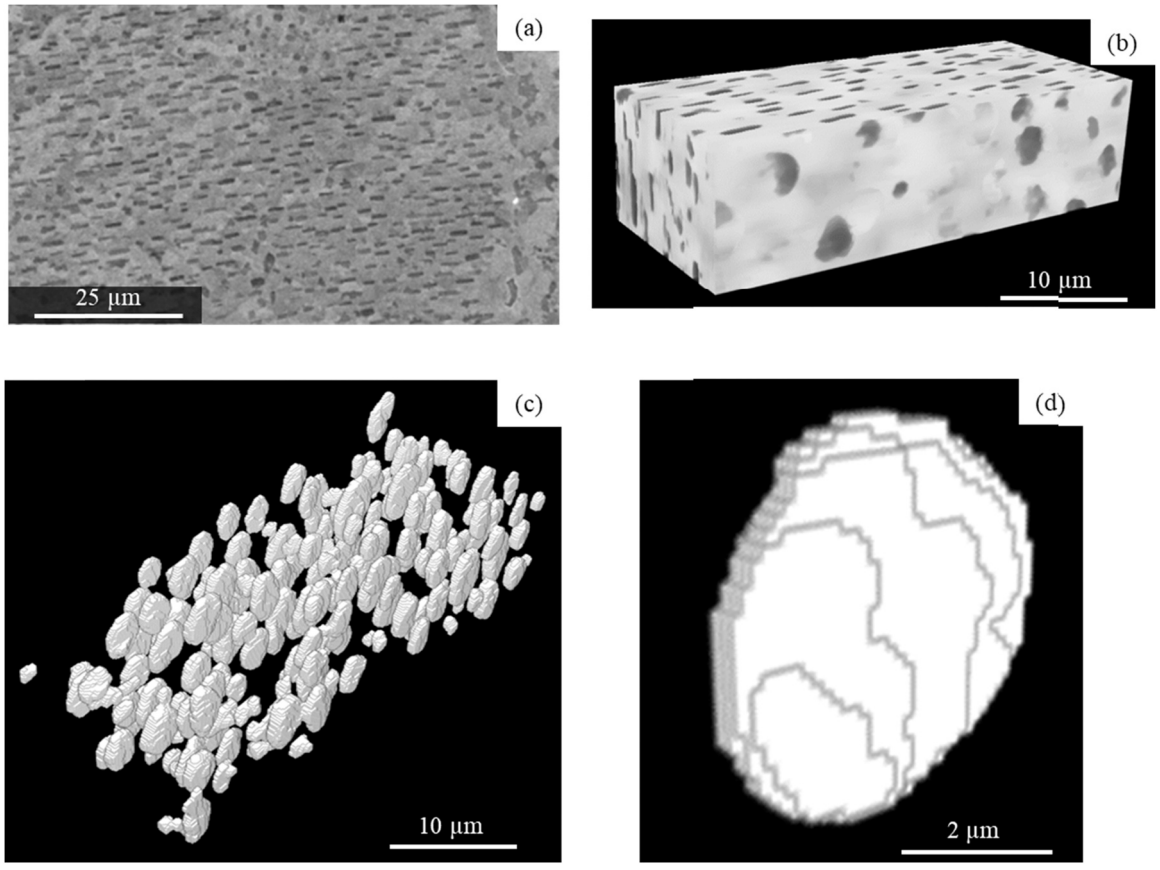

Fig. 3. 3D view of the precipitates in the initially statically recrystallized grains. (a) A region of interest which contains the "rectangular" precipitates in 2D, (b) a processed stack of 2D images of a sub-volume extracted from (a) taken at 0.1 μm successive serial sectioning using FIB milling, (c) the same region as (b) after segmentation of the precipitates, and (d) a higher magnification view of a single precipitate.

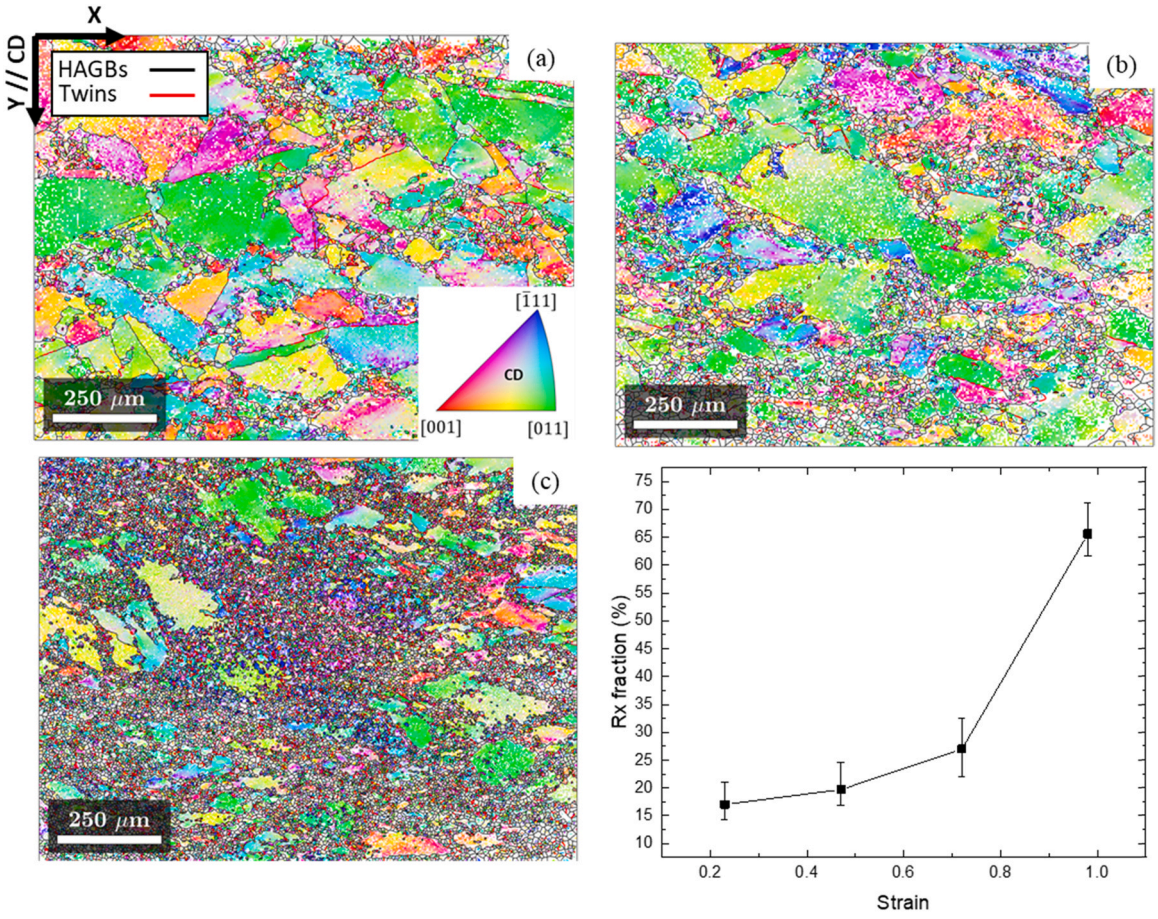

Fig. 4. Effect of local strain on microstructure evolution - (a) $\varepsilon \approx 0.23$, (b) $\varepsilon \approx 0.72$, and (c) $\varepsilon \approx 0.98$. The step size for the EBSD maps in (a) through to (c) were 4 µm, 4 µm and 2.5 µm, respectively. (d) A plot of the area fraction of recrystallized grains as a function of strain. The compression direction (CD) is vertical, as indicated.

the form of geometrically necessary dislocations. They display a relatively high density of fine, spherical precipitates which are similarly coherent with their host grain (i.e., a misorientation angle of ≤ 0.5°). Note this is somewhat different from the strict crystallographic definition of the term coherent. These unrecrystallized grains have persisted through the first steps of the ingot to billet conversion process, and are referred to as "initially unrecrystallized grains" hereafter.

(iii) Small recrystallized grains - these are small grains (equivalent diameters ≈ 3.2 µm) with low internal KAM values, indicating low internal misorientations and low stored energy. These grains show a mixture of rather large intragranular precipitates which are coherent with their host grain, and intergranular precipitates at their boundaries with the initially unrecrystallized grains. This third type of grain occupies a relatively low area fraction of the microstructure compared to the former two types of grain. Additionally, this grain type does not exhibit any very specific precipitation state that could be unambiguously recognised after subsequent deformation. Therefore, the dynamic recrystallization behaviour of only the former two types of grain will be described in the following; the behaviour of these small recrystallized grains during hot deformation will not be addressed.

The results of precipitate characterisation in the different grain populations are provided in Table 3 and Fig. 2(g). An average equivalent circle diameter value and an area density (i.e., the number of particles per µm^2) are quoted in Table 3. For the precipitates in the initially statically recrystallized grain, the maximum Feret diameter is also included. This approximately corresponds to the long axis of the rectangles seen in 2D sections in these grains, and so gives a measure of their length.

Fig. 3 shows the results of the nano-tomography performed with the FIB-SEM, to reveal the 3D geometry of the "rectangular" precipitates in the initially statically recrystallized grains. In 3D, these precipitates in fact have the shape of a disc, or a flat cylinder, although they appear rectangular in 2D cross-sections [27]. The diameter of the precipitate shown in Fig. 3(d) is ~ 4.1 µm and the thickness is ~ 0.6 µm. Calculating an equivalent circle diameter based on the area of the rectangular 2D sections of these precipitates is thus likely to produce an underestimate of their actual diameter. The maximum Feret diameter of the "rectangular" precipitates is likely to be a more relevant parameter, hence its inclusion in Table 3. Note that a particular mechanism leading to the formation of precipitates with this shape has been proposed in the literature [26,27].

Fig. 4 shows IPF maps with respect to the compression direction of the microstructure at different locations of the deformed sample, corresponding to different local strain levels, following compression. These are relatively large area maps, acquired using a large step size (2.5–4 µm). Given the large step size, these maps do not show fine microstructural details (i.e., accurate shapes of the recrystallized grains) though they do provide an overall picture of the microstructure and the progression of recrystallization. The size, shape and orientation of the large deformed grains, which have not undergone recrystallization, can be inspected from these orientation maps. Fig. 4(d) shows a plot of recrystallized fraction as a function of strain. In these maps, recrystallized and unrecrystallized grains were separated based on grain size. Grains with an equivalent radius

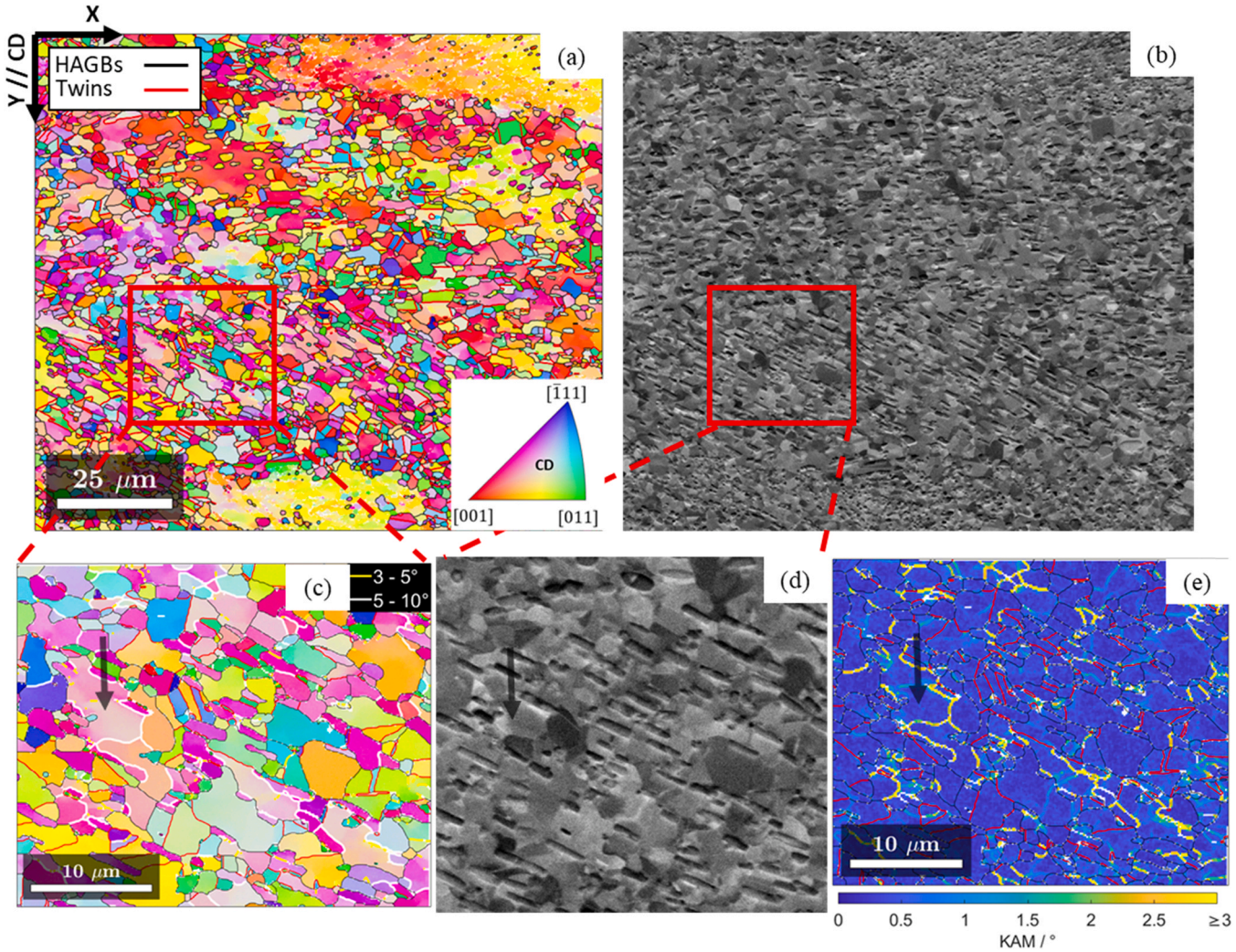

Fig. 5. Onset of intragranular recrystallization in the initially statically recrystallized grains. (a) An IPF map of an area containing fragments of an initially statically recrystallized grain, (b) FSE micrograph of the same area in (a). (c), (d) and (e) respectively show an IPF map, FSE micrograph and KAM map for the region enclosed by the red rectangle in (a) and (b). LAGBs and MAGBs are indicated by yellow and white lines in (c). The black arrow indicates a remaining fragment of the initially statically recrystallized grain. This area corresponds to region 3 in Table 2, where the local strain was $\varepsilon \approx 0.76$.

greater than 10 μm were classed as recrystallized, and those above as unrecrystallized. This threshold was decreased to 8 μm and increased to 15 μm to produce the error bars in Fig. 4(d). This approach is similar to the one used by Eriksson et al. [13]. The relatively high recrystallization levels at low strains can be attributed to the fact that the as-received microstructure was partially recrystallized, and it already contained stored energy (notably within the initially unrecrystallized grains).

Fig. 4(c) shows that even at the highest local strain level analysed, unrecrystallized grains remain. This raises the question of whether these grains are remnants of the initially unrecrystallized grains of the as-received material, or deformed fragments of the initially statically recrystallized grains, whose lower initial stored energy may have been a kinetic disadvantage for recrystallization. The progress of recrystallization in each of these populations, recognised based on their γ' morphology, are analysed for different local strain levels in the following.

3.2. Recrystallization around the initially statically recrystallized grains

Fig. 5 shows a region corresponding to region 3 in Table 2 with a local strain level of $\varepsilon \approx 0.76$. This region must have contained an initially statically recrystallized grain prior to deformation, as indicated by the "rectangular" precipitates seen in Fig. 5(b). However, the IPF map in Fig. 5(a) and the KAM map in Fig. 5(e) show that this initially statically recrystallized grain has almost completely recrystallized, with only small fragments of the original grain remaining. One such fragment is indicated in Fig. 5(c). Inspecting this small fragment of the initially statically recrystallized grain reveals that LAGBs (plotted yellow) and MAGBs (plotted white) have formed intragranularly. The KAM map for this area (Fig. 5(e)) shows that geometrically necessary dislocations within this fragment are strongly concentrated at these intragranular sub-boundaries. This suggests that the initially statically recrystallized grains can recrystallize via a continuous process which involves intragranular dislocation polygonisation, forming regions which are initially walled off by LAGBs. As more dislocations accumulate, these LAGBs progressively become MAGBs and eventually HAGBs. These LAGBs and MAGBs can form around the existing precipitates, allowing the precipitates to persist through recrystallization.

Fig. 6 was taken from an area where the local strain was $\varepsilon \approx 1.00$ (corresponding to region 4 in Table 2) and shows that the characteristic shapes and orientations of the "rectangular" precipitates in the initially statically recrystallized grains are preserved throughout deformation and DRX of their host initially statically recrystallized grains. In Fig. 6(a), the "rectangular" precipitate indicated by the red

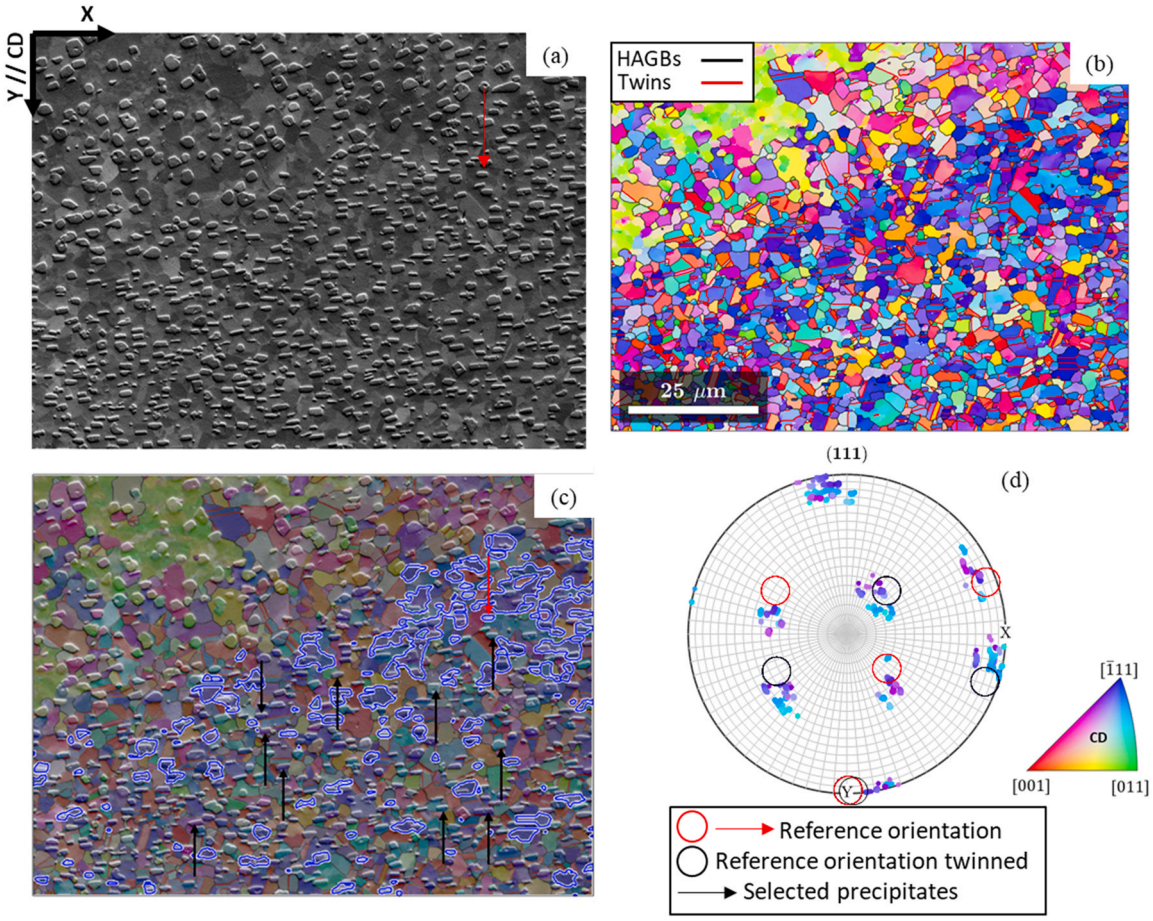

Fig. 6. Crystallographic orientation of "rectangular" precipitates in region 4 from Table 2, where $\varepsilon \approx 1.00$. (a) A FSE micrograph of a region which contained an initially statically recrystallized grain prior to deformation, (b) the corresponding IPF map depicting that the initially statically recrystallized grain has dynamically recrystallized following deformation. (c) The FSE micrograph in (a) with a partially transparent overlay of the IPF map and (d) a {111} polefigure of a selection of 10 grains indicated by black arrows in (c) containing "rectangular" precipitates with orientations outwith 10° of the reference precipitate highlighted by the red arrow in (c). Note that the reference orientation (red circles) and one of its twin orientations (black circles) are highlighted in (d). The blue lines in (c) outline grains with orientations within 10° of the reference orientation.

arrow was taken as a reference orientation. All grains with orientations within 10° of this reference are highlighted with a blue outline in Fig. 6(c). This shows that many "rectangular" precipitates, or the small recrystallized grains hosting them, have an orientation close to that of the reference, indicating that their orientation has been preserved throughout deformation and recrystallization. This reference orientation is shown by the red circles on the pole figure in Fig. 6(d). A selection of 10 grains containing "rectangular" precipitates which do not satisfy the 10° condition are indicated with black arrows in Fig. 6(c), labelled as "selected orientations". Their orientations are also plotted on the pole figure in Fig. 6(d). These precipitates either have small misorientations to the reference orientation (i.e., they appear close to the red circles corresponding to the reference orientation), or have an approximately twin orientation relationship with the reference orientation and appear close to the black circles, which show an orientation that is twin related to the reference orientation. Since a given initially statically recrystallized grain can contain both close to coherent and close to twin precipitates [26], this confirms that these precipitates retain their initial orientations through recrystallization.

Additionally, recrystallization can be seen to occur immediately around the relatively large "rectangular" γ' particles in the initially statically recrystallized grains. Some examples of this are presented in Fig. 7. These were taken from an area where the calculated local strain was $\varepsilon \approx 1.04$, corresponding to region 5 in Table 2. These examples show the indicative features of the hetero-epitaxial recrystallization (HERX) mechanism. HERX is a recently characterised DRX mechanism, in which a coherent shell of γ phase precipitated around a γ' particle acts as recrystallization nucleus. Recrystallized grains which have undergone this mechanism are expected to contain a single, close to coherent γ' precipitate [17,18], as is indeed the case for the grains highlighted in Fig. 7.

3.3. Recrystallization of the initially unrecrystallized grains

In total, four different recrystallization processes were observed to occur in/around the initially unrecrystallized grains, giving rise to four distinguishable types of recrystallized grain. These different groups of grains are highlighted in Fig. 8, which comes from an area with a calculated local strain of $\varepsilon \approx 0.72$, corresponding to region 2 in Table 2. The vast majority of the recrystallized grains are found at the boundaries of the initially unrecrystallized grains, are small, have low intergranular misorientations (indicated by their low KAM values) and display little to no intragranular precipitation. These grains form a typical necklace structure around the initially unrecrystallized grains. Such recrystallized grains will be referred to as "necklace recrystallized grains" hereafter.

In addition to these necklace recrystallized grains, a second population of recrystallized grains which are larger, contain rectangular precipitates and display higher internal KAM values can also be found within the necklace structure. Examples of these are indicated by the yellow arrows in Fig. 8(a) and (b). The average equivalent diameter of the recrystallized grains surrounding the initially unrecrystallized grain on the right-hand side of Fig. 8(a) is 2.7 μm, and

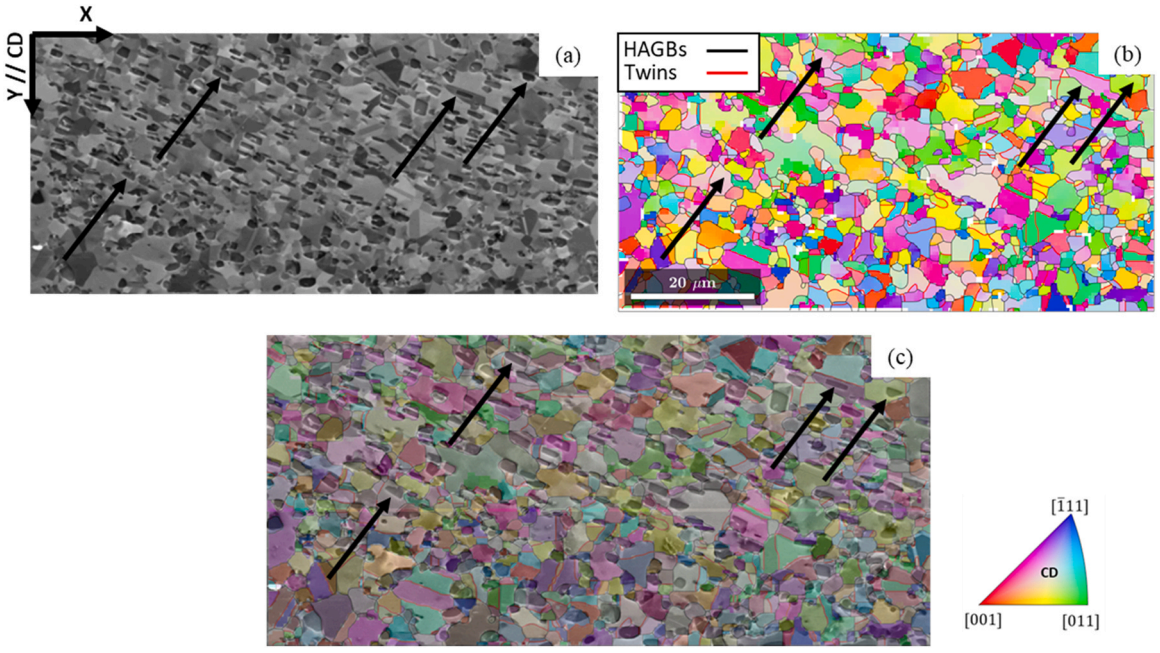

Fig. 7. Examples of HERX within an initially statically recrystallized grain, from region 5 in Table 2, where $\varepsilon \approx 1.04$. (a) A BSE micrograph with four "rectangular" precipitates indicated by black arrows, (b) a corresponding IPF map confirming that these precipitates are the only ones within their grains, and (c) a transparent version of the IPF map overlaid onto the BSE micrograph to ease visualisation.

those of the large recrystallized grains highlighted by the yellow arrows are 13.8 µm and 11.0 µm. These will be referred to as "large recrystallized grains" or "large recrystallized grains containing rectangular precipitates" hereafter.

Thirdly, intragranular "channels", indicated by the red arrows in Fig. 8(a) and (b), can be identified. These regions have a slight misorientation to their surrounding initially unrecrystallized grain (as shown by the KAM maps), a lower density of precipitation than the surrounding initially unrecrystallized grain and slightly lower internal KAM values, though not as low as seen in the recrystallized regions. Finally, a grain which is likely to have undergone HERX can be identified.

Fig. 8(e) shows an IPF Z map (as opposed to the IPF Y map in Fig. 8(a)), which confirms that the initially unrecrystallized grains at the centre and to the right of the region in Fig. 8 have very similar orientations (with a misorientation angle of 7.7° between their mean orientations). As such they may have previously been a single grain, which has now been split into two parts due to intragranular recrystallization. Inside the recrystallized region separating these two grains a recrystallized grain containing rectangular precipitates can also be identified (highlighted by the orange arrow).

Fig. 9 highlights the formation of the necklace recrystallized grains, by showing sub-grains forming at the periphery of an initially unrecrystallized grain. LAGBs are indicated by yellow lines in Fig. 9 and MAGBs are indicated by white lines. The sub-grains are separated from the neighbouring initially unrecrystallized grains by MAGBs, shown in Fig. 9(b) and (f). The FSE micrographs shown in Fig. 9(a) and (d) reveal that the sub-grains are free from intragranular precipitation. The KAM maps in Fig. 9(c) and (g) show that the sub-grains have low internal misorientations. They progressively develop into necklace recrystallized grains when the misorientation of the boundary between them and the neighbouring initially unrecrystallized grain increases beyond 10°. This misorientation angle progressively increases as more and more dislocations are incorporated into the boundary during deformation. Bearing in mind the defining features of these necklace recrystallized grains, the following can be suggested as their formation mechanism:

During deformation, sub-grains form close to the existing boundaries of initially unrecrystallized grains due to the higher local dislocation densities near the grain boundaries, which are a consequence of plastic incompatibility between neighbouring grains. Further deformation leads to the migration of mobile sub-grain boundaries, which absorb additional dislocations as they migrate, increasing their misorientation angle with their parent grains. These moving sub-grain boundaries may dissolve the precipitates they encounter [28]. Once a sufficiently high misorientation angle is achieved the sub-grain becomes a recrystallized grain with a HAGB between it and the initially unrecrystallized parent grain. Eventually, the boundaries of the newly recrystallized grain become saturated with γ' forming elements, and its growth is halted due to a combination of solute drag and pinning from further precipitates encountered in the initially unrecrystallized parent grain.

This process accounts for the observed differences in precipitation between initially unrecrystallized and necklace recrystallized grains. During the formation of necklace recrystallized grains, precipitates are dissolved into the migrating sub-grain boundaries. When the grain is fully developed, it will likely be surrounded by other recrystallized grains which have formed by a similar mechanism at the boundary of the initially unrecrystallized grain, and precipitation can occur at their shared boundaries. Fast diffusion through the saturated boundaries allows for these precipitates to coarsen, giving rise to the relatively large precipitates (i.e., with equivalent diameters of 2.1–3.1 µm based on the recrystallized regions in Fig. 8(b)) seen at the boundaries of the necklace recrystallized grains. The intergranular precipitates between the necklace recrystallized grains show no special orientation relationship to their surrounding grains.

Microstructures of large recrystallized grains containing rectangular precipitates are shown in Fig. 10, which highlights the misorientation angles between these grains and their neighbouring initially unrecrystallized grains. For all cases, the misorientation angles were high (> 50°), with one exception highlighted with a red arrow. The grain with the lower misorientation contains precipitates which are approximately coherent with it (i.e., misorientation angle < 1°), while those with the higher misorientations (indicated

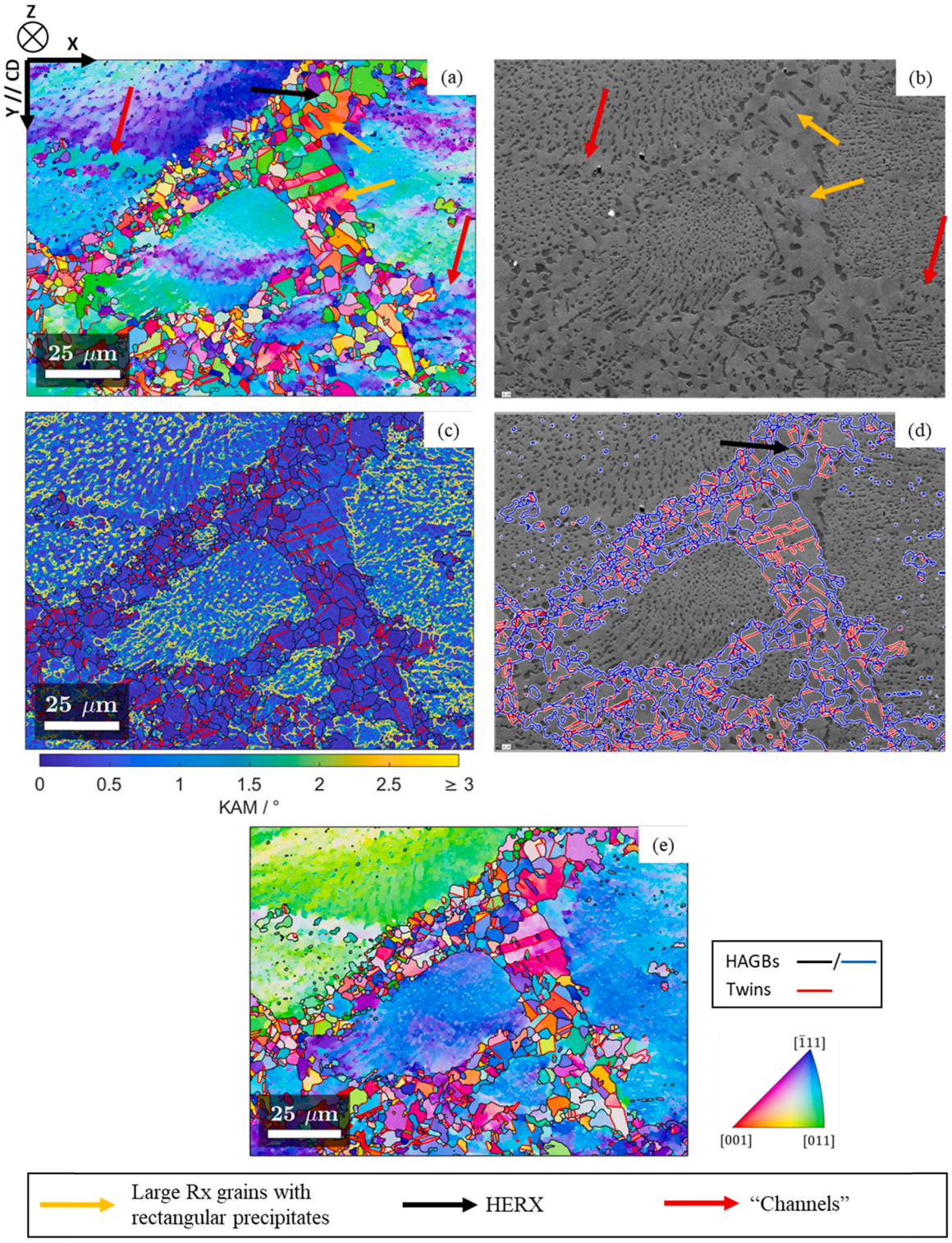

Fig. 8. Overview of the different recrystallization mechanisms occurring around and within an initially unrecrystallized grain (region 2 in Table 2, where $\varepsilon \approx 0.72$). (a) An IPF Y map, (b) corresponding FSE micrograph, (c) KAM map, (d) the FSE image with the grain boundaries overlaid, and (e) an IPF Z map.

by the black arrows) contain precipitates which have approximately twin orientation relationships with their host grains (corresponding to red boundaries in (a) and (b)).

To inspect the orientation relationships between the large recrystallized grains, their rectangular precipitates, and their neighbouring initially unrecrystallized grains further, (111) pole figures for all three are plotted in Fig. 11. Fig. 11(b) and (d) show that there is a shared < 111 > axis between the large recrystallized grains, their rectangular precipitates, and the neighbouring initially unrecrystallized grain. This axis is outlined by the red circle in Fig. 11(b) and (d).

As the large recrystallized grains with rectangular precipitates have a number of distinguishing features which separate them from the necklace recrystallized grains, a different mechanism may have resulted in their formation. Similar grains, i.e., large recrystallized grains containing close to twin or close to coherent precipitates

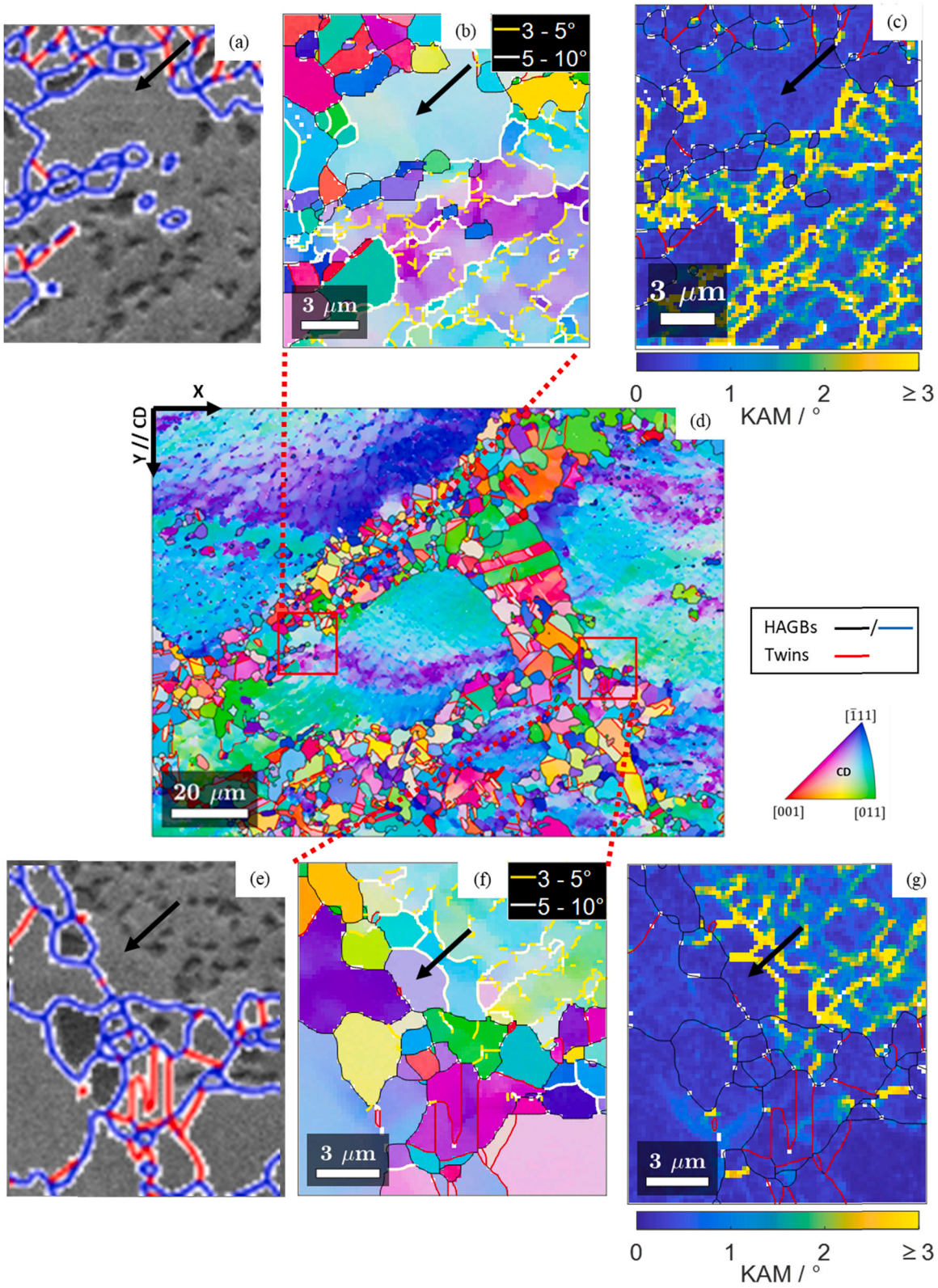

Fig. 9. The formation of sub-grains at the boundaries of the initially unrecrystallized grains (from region 2 in Table 2, where $\varepsilon \approx 0.72$). (a), (b) And (c) respectively show a FSE micrograph with overlaid grain boundaries, an IPF map, and a KAM map of an area highlighted in (d), which is an IPF map of an area containing initially unrecrystallized grains. (e), (f) and (g) show similar information to (a), (b) and (c), respectively, but for a separate area in (d).

displaying a rectangular shape in 2D sections, have been observed to form *statically* in AD730 and other alloys by Vernier et al. [26], but here they appear to form dynamically.

Vernier et al. showed that in order to overcome the relatively fine and dense precipitation in initially unrecrystallized grains, it is advantageous for the growing recrystallized grain to approximately

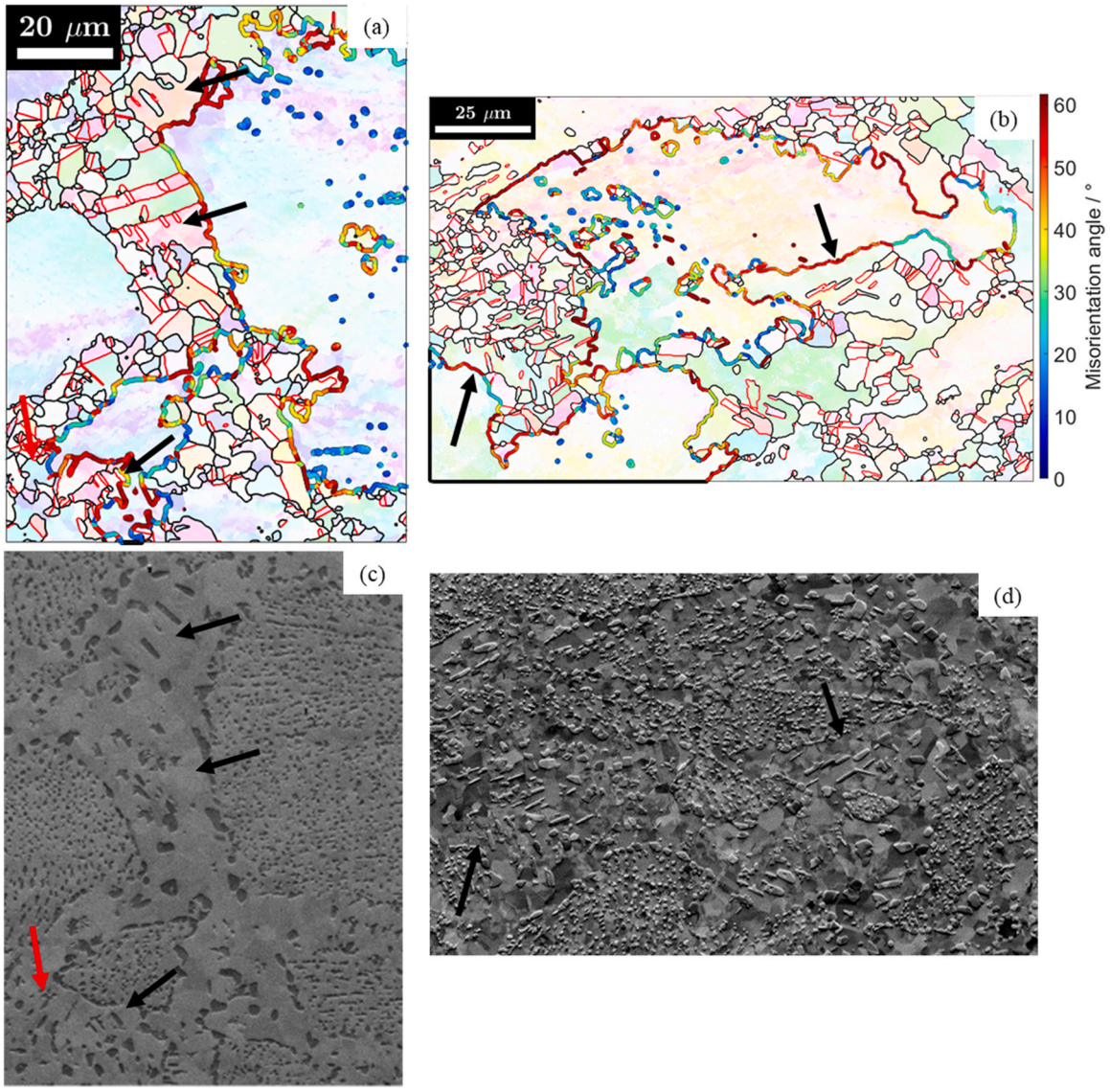

Fig. 10. Misorientation angles between the large recrystallized grains and their neighbouring initially unrecrystallized grains. (a) And (b) EBSD grain boundary maps of two initially unrecrystallized grains, colourised according to their local boundary misorientation angle. The positions of selected large recrystallized grains containing rectangular precipitates are indicated by the black arrows. These recrystallized grains tend to show high misorientations with the initially unrecrystallized grain (> 50°), although the grain indicated by the red arrow shows a lower misorientation. (c) And (d) FSE micrographs of the same regions as those of (a) and (b), respectively, where the rectangular precipitates are evident. (b) And (d) are from region 1 in Table 2 with a local strain of $\varepsilon \approx 0.53$, (a) and (c) are from region 2 in Table 2 with a local strain of $\varepsilon \approx 0.72$.

share a < 111 > axis with the initially unrecrystallized grain. This facilitates a growth mechanism which overcomes precipitates in the initially unrecrystallized grain and produces rectangular precipitates in the growing recrystallized grain with an approximately twin or approximately coherent orientation relationship to the growing recrystallized grain [26]. Twin precipitates were observed to form when there was a larger misorientation angle between the recrystallized and initially unrecrystallized grains ($\gtrsim 50°$), coherent ones when there was a smaller misorientation angle between them ($\lesssim 37°$), and a mixture of both for grains with intermediate misorientation angles. In the present case, with the recrystallized grains forming *dynamically,* the common < 111 > axis has been demonstrated in Fig. 11. Additionally, consistent with previous observations, the tendency for twin related precipitates to form in the case of higher misorientation angles, and coherent ones in the case of lower misorientation angles is demonstrated in Fig. 10.

The formation of the large recrystallized grains containing rectangular precipitates is thus thought to be rather similar to their formation in static recrystallization. When a recrystallized grain approximately shares < 111 > axis with a neighbouring initially unrecrystallized grain, it can grow by consuming the initially unrecrystallized grain and its precipitation. Reprecipitation occurs in the form of rectangular precipitates with a close to twin or close to coherent orientation relationships to the recrystallized grain. Reprecipitation was observed to occur at the interface between the recrystallized and initially unrecrystallized grains in [26], and it is likely that this is also the case in this study.

Alongside the two types of recrystallization observed along the former grain boundaries, a form of intragranular recrystallization was also seen inside the initially unrecrystallized grains (see Fig. 12). Fig. 12(a)–(d) show long “channels” within the initially unrecrystallized grains, which exhibit a very low density of precipitates, and lower KAM values on their interior than the surrounding initially unrecrystallized grain. The precipitates at the edges of such a channel are slightly coarser than elsewhere in the grain, suggesting that the precipitates previously present within the channel could have been dissolved and reprecipitated at their edge. In Fig. 12(f) a band of recrystallized grains within an initially

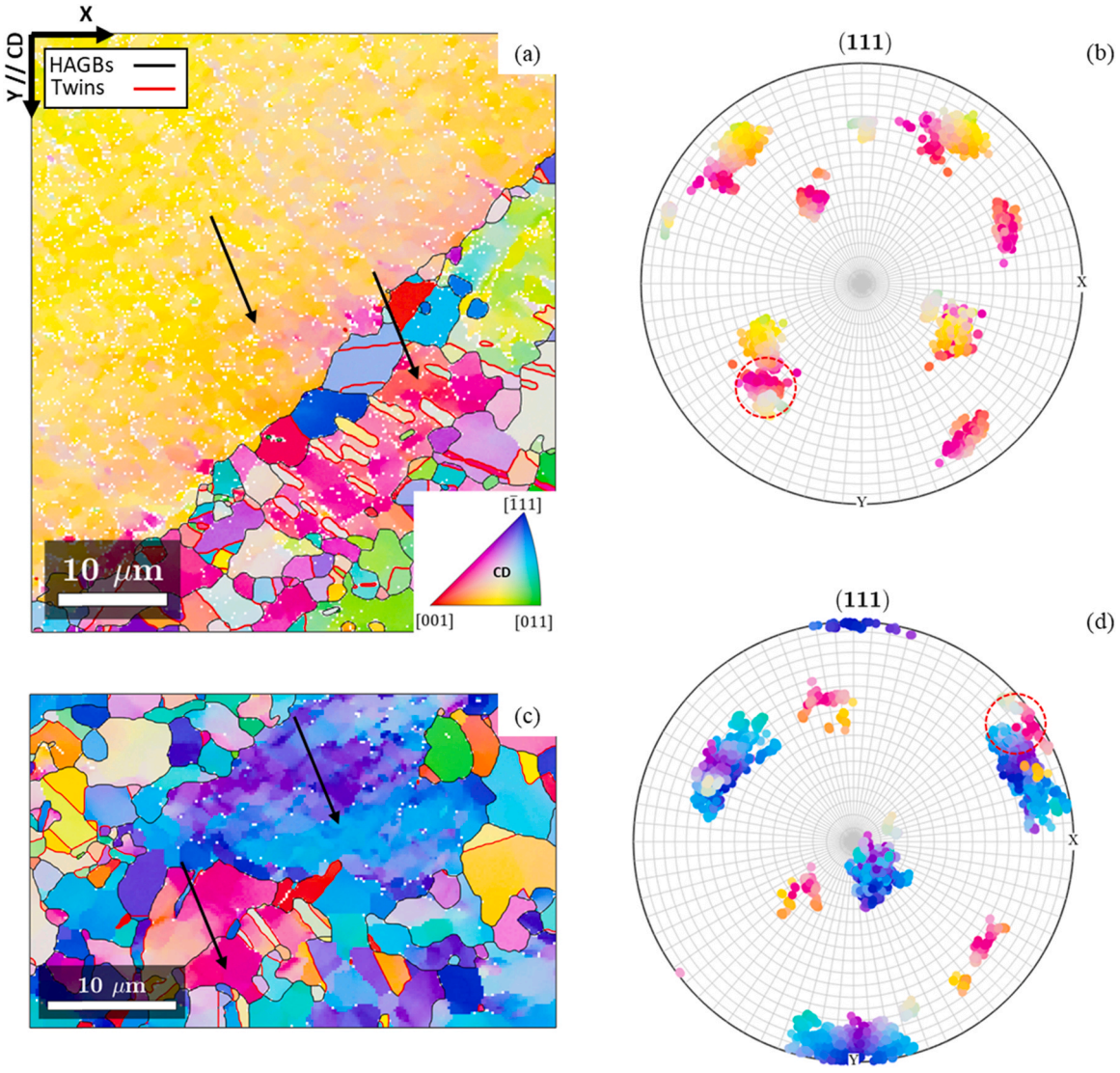

Fig. 11. Orientation relationships between two large recrystallized grains, their rectangular precipitates and their neighbouring initially unrecrystallized grains. (a) And (c) IPF maps containing a large recrystallized grain and neighbouring initially unrecrystallized grain indicated by black arrows, (b) and (d) corresponding {111} pole figures for the large recrystallized grain, its rectangular precipitates and the initially unrecrystallized grain. The red dashed circles in (b) and (d) enclose the {111} pole which is common to all three. The grid on (b) and (d) corresponds to an angular spacing of 5°. (a) And (b) are from region 1 in Table 2 with a local strain of $\varepsilon \approx 0.53$, (a) and (c) are from region 2 in Table 2 with a local strain of $\varepsilon \approx 0.72$.

unrecrystallized grain, adjacent to one of the channels, is highlighted by a black arrow.

Looking at the misorientation profiles within such channels in Fig. 12(e)–(h), it is evident that sub-grain boundaries have formed within the channels, generating point to point orientation changes of larger than 2°. These sub-grain boundaries could progressively increase their misorientation to become HAGBs, and create a band of intragranular recrystallized grains, such as the one shown by the black arrow in Fig. 12(g). The interiors of the recrystallized grains indicated in Fig. 12(g) are free from precipitation, showing that the formation of the channels is accompanied by local precipitate dissolution.

Plastic flow inhomogeneity within the initially unrecrystallized grains could play a role in the formation of such channels. Here, dislocations within certain regions of the initially unrecrystallized grains would be more active, and could move to arrange themselves into LAGBs. Whilst doing so, the dislocations could assist in the dissolution of the precipitates they encounter, giving rise to precipitate free channels bordered by LAGBs within the initially unrecrystallized grains. Dislocation assisted dissolution of γ' and subsequent recrystallization in a Ni-based superalloy has recently been observed [40]. In Fig. 13, two regions within initially unrecrystallized grains, where local precipitate dissolution has occurred, are highlighted. Such regions could go on to form the recrystallized channels. This would imply that precipitate dissolution precedes the formation of LAGBS during the formation of such "channels".

The formation of these "channels" presents an important recrystallization effect, in the sense that they can span considerable lengths within a grain, and significantly reduce the size of the initially unrecrystallized grains. One such channel could effectively split an initially unrecrystallized grain in half. In Fig. 12(b), the total length of the band of intragranular recrystallized grains and the adjacent channel is approximately 75 μm. The recrystallized region separating the two similarly orientated initially unrecrystallized grains in Fig. 8 could have originated from such a channel.

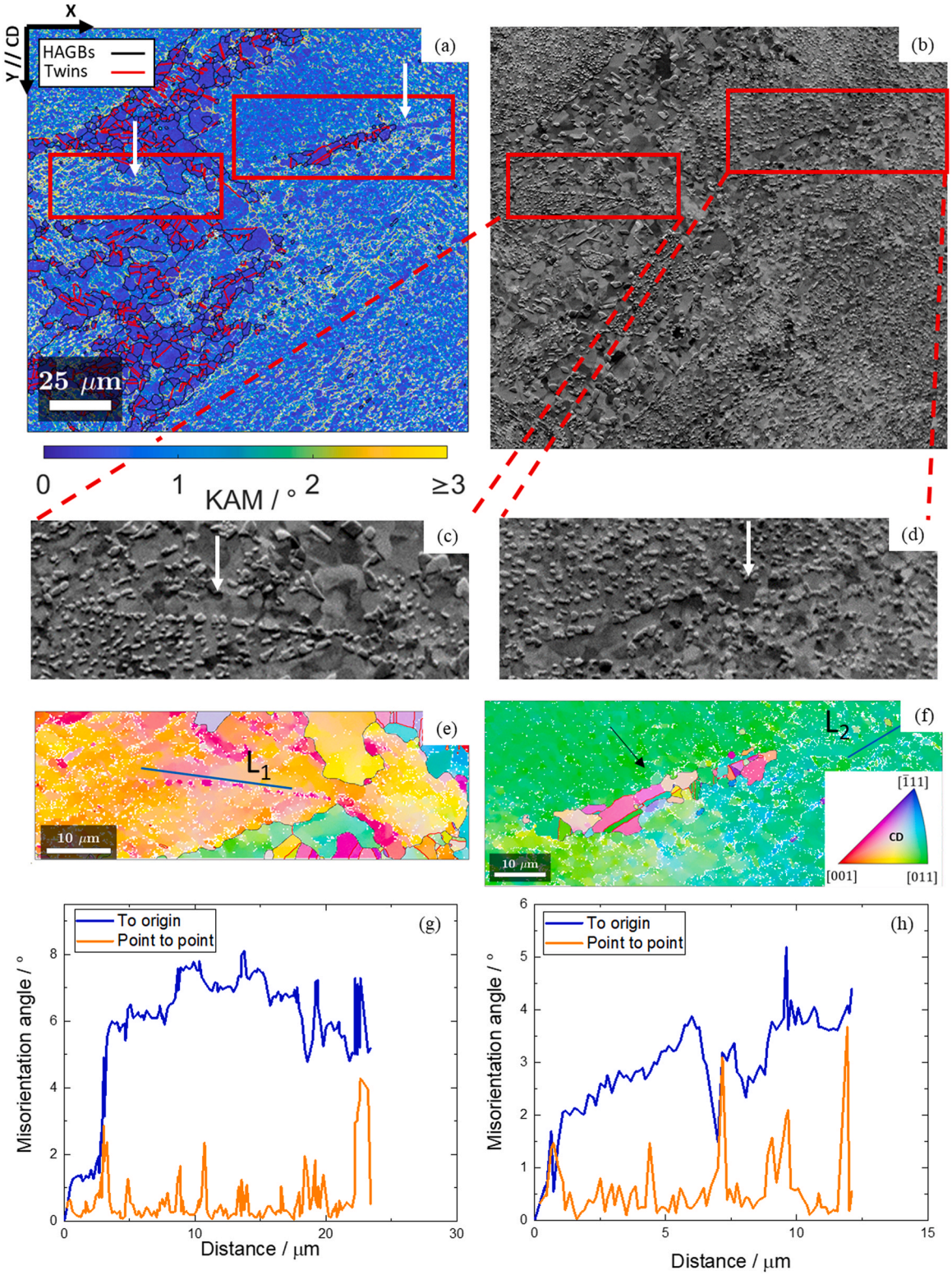

Fig. 12. Intragranular recrystallization in the initially unrecrystallized grains. (a) A KAM map depicting two low KAM "channels" within initially unrecrystallized grains highlighted by white arrows in the red rectangles. (b) Corresponding FSE micrograph, (c) and (d) are higher magnification FSE micrographs of the low KAM channels where the white arrows indicate the "channels". (e) And (f) are IPF maps of the areas shown in (c) and (d), the black arrow in (f) highlights a band of recrystallized grains within the initially unrecrystallized grain. (g) And (h) are misorientation profiles taken along the blue lines L_1 and L_2, respectively, showing both 'point to point' and 'point to origin' misorientations. Data from region 1 in Table 2 with a local strain of $\varepsilon \approx 0.53$.

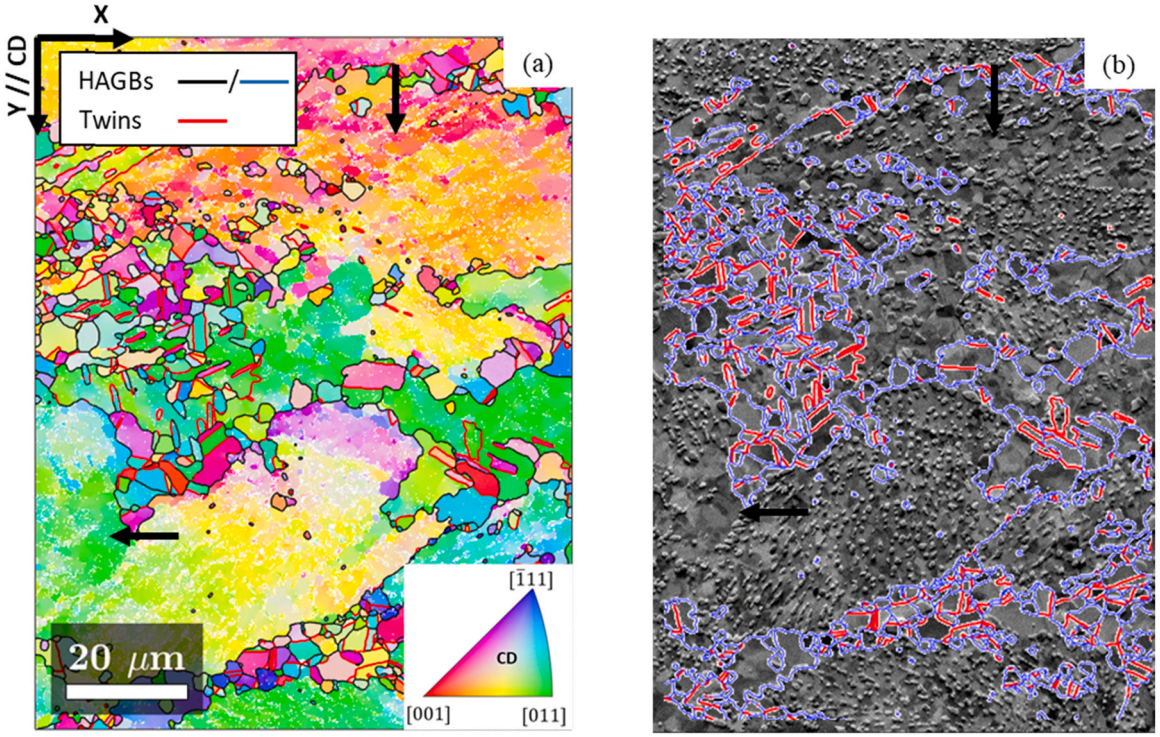

Fig. 13. Examples of inhomogeneous precipitation within the initially unrecrystallized grains. (a) IPF map and (b) the corresponding FSE micrograph of an area containing two regions within initially unrecrystallized grains where there has been a local dissolution of precipitates, these regions are indicated by the black arrows. The grain and twin boundaries from (a) have been overlaid onto (b). Data from region 1 in Table 2 with a local strain of $\varepsilon \approx 0.53$.

4. Discussion

4.1. Recrystallization in the initially unrecrystallized grains

Around and within a single initially unrecrystallized grain, up to four DRX processes operate simultaneously, generating distinguishable populations of recrystallized grains. The distinguishing features of these populations have been highlighted, and formation mechanisms consistent with these observations were proposed.

Grain boundary bulging is one of the most commonly invoked mechanisms to explain the formation of recrystallized grains near grain boundaries. However, its role in the formation of the necklace recrystallized grains is not clear. The most common explanation of grain boundary bulging is that of Belyakov [41], where plastic incompatibility between neighbouring grains gives rise to boundary serration. This leads to boundaries interlocking and eventually preventing further boundary sliding or shearing, so dislocations build up near the boundary. This high dislocation density leads to the formation of sub-grains and eventually recrystallized grains near the boundary [42]. Here, the new recrystallized grain will have an orientation similar to the host initially unrecrystallized grain.

Grain boundary bulging is not necessarily involved in the formation of the necklace recrystallized grains. There are instances of sub-grains forming adjacent to entirely flat boundary sections, such as Fig. 9(e)–(g), and instances of sub-grains which are adjacent to bulged boundaries, shown in Fig. 14. The formation of recrystallized grains and sub-grains next to flat boundary sections has also been observed during recrystallization of Haynes 282 above its γ' solvus temperature [13].

In the cases where sub-grains have been observed to form next to a flat grain boundary section (e.g., Fig. 9(e)–(g)), it is possible that either high dislocation densities were generated near the boundaries without bulging, or that the apparently flat boundary sections are in fact serrated when viewed in 3D but do not appear as such in the particular 2D section observed.

It has previously been argued that grain boundary bulging could only occur at the interface between two large grains, as a very high curvature would be needed for bulging from a small recrystallized grain [19]. As such, during the formation of a typical necklace DRX microstructure, bulging would only occur for the first “ring” of recrystallized grains, forming at the interface between two large initially unrecrystallized grains. However, the opposite has also been argued, that bulging occurs during all stages of the development of a necklace microstructure, even at an interface featuring a small recrystallized grain [43]. In the present case, the most obvious bulges are indeed found at the interface between large unrecrystallized grains; this is highlighted in Fig. 14. At the interface between small recrystallized grains and large initially unrecrystallized grains, recrystallization nuclei can be seen to form without bulging (e.g., the sub-grain highlighted in Fig. 9(e)–(g)). This evidence would tend to support the former view, that bulging predominately occurs at the interface between large grains.

The abundance of the grain boundary recrystallization mechanism leading to necklace recrystallized grains is indicated in Fig. 15, which shows the misorientation angle distributions around the boundary of an initially unrecrystallized grain. The disproportionately high fraction of lower angle boundaries around the initially unrecrystallized grain suggests that the majority of recrystallized grains surrounding the initially unrecrystallized grain form as necklace recrystallized grains, which is consistent with the precipitation state found in these recrystallized regions. This indicates that this grain boundary recrystallization mechanism, which may occur with or without bulging, is the most abundant mechanism during sub-solvus forging. The misorientation angle distribution also shows a sharp peak around 60°, suggesting that twinning occurs within the necklace recrystallized grains during their formation and evolution. Twin assisted nucleation of dynamically recrystallized grains has been observed in IN718 [44]. Twining may further assist the growth of recrystallized grains by forming highly mobile grain boundaries [45,46].

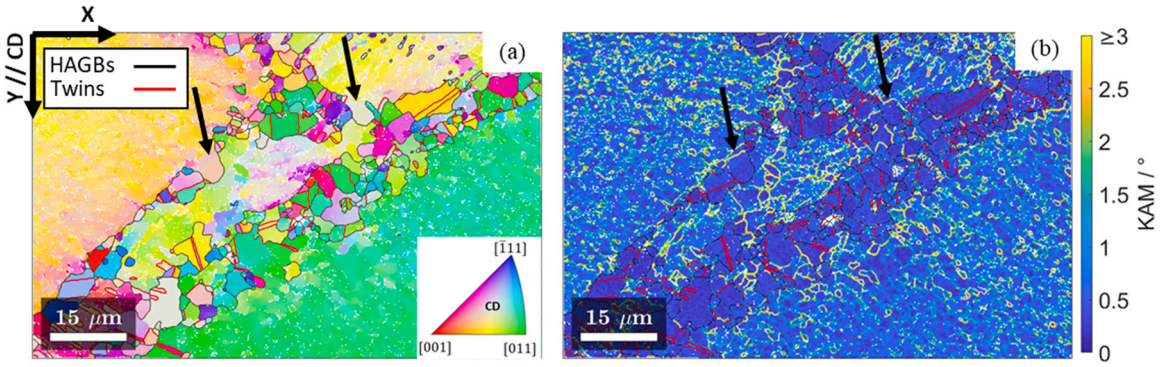

Fig. 14. The formation of sub-grains at bulged grain boundaries. (a) Two bulged grain boundaries indicated by the black arrows, and (b) the corresponding KAM map showing that the regions within the bulges have low internal misorientations. Data from region 1 in Table 2 with a local strain of $\varepsilon \approx 0.53$.

4.2. Recrystallization around the initially statically recrystallized grains

Fig. 6 shows that the orientation and morphology of the special type of precipitates found in the initially statically recrystallized grains were unchanged during deformation and DRX. This indicates that DRX can occur in these grains without the dissolution/re-precipitation of precipitates, the opposite of what has been observed in the initially unrecrystallized grains. Regarding the size of these precipitates, counting 470 of the "rectangular" precipitates from Fig. 6(a) gives an equivalent diameter of 1.3 ± 0.5 μm and an area fraction of 18.5%. This diameter and area fraction are smaller than those measured in the as-received microstructure (1.8 ± 0.7 μm and 21.7%). It is not clear from the measurements of diameter alone whether the size of these precipitates has actually decreased, as this could be an artefact due to the particular 2D section of the precipitates being imaged. However, the corresponding decrease in area fraction suggests that these precipitates have actually shrunk somewhat during recrystallization, perhaps due to partial dissolution by the grain boundaries forming around and between them.

Intragranular recrystallization in the initially statically recrystallized grains is further assisted by HERX, of which examples can be seen in Fig. 7.

4.3. The role of microstructural heterogeneity

Different recrystallization mechanisms are operative in the initially unrecrystallized and the initially statically recrystallized grains. These different mechanisms are a consequence of the different precipitation states in the two types of grain, i.e. they are a consequence of microstructural heterogeneity. The fine and dense distribution of precipitates in the initially unrecrystallized grains restrict dislocation motion, and the nucleation of new recrystallized grains is restricted predominately to the grain boundaries, where dislocation densities are highest. By way of contrast, in the initially statically recrystallized grains recrystallization occurs predominately intragranularly as dislocations can progressively accumulate into low/medium angle boundaries, less impeded by the more coarse and sparse distribution of precipitates.

These different recrystallization mechanisms, which operate in different grain populations as a result of microstructural heterogeneity, have two important effects.

Firstly, the different mechanisms affect the overall kinetics of recrystallization. Figs. 6 and 7 show that at regions with estimated strains of 1.00–1.04, the initially statically recrystallized grains are almost fully recrystallized. However, from Fig. 4, the overall recrystallization level at this strain is approximately 65%. Therefore, at high strains only the initially unrecrystallized grains remain unrecrystallized. The initially statically recrystallized grains undergo recrystallization more easily (i.e. at lower strains) than the initially unrecrystallized grains, due to their different recrystallization mechanisms. These different mechanisms are a result of the different local precipitate distributions in the initially statically recrystallized and initially unrecrystallized grains.

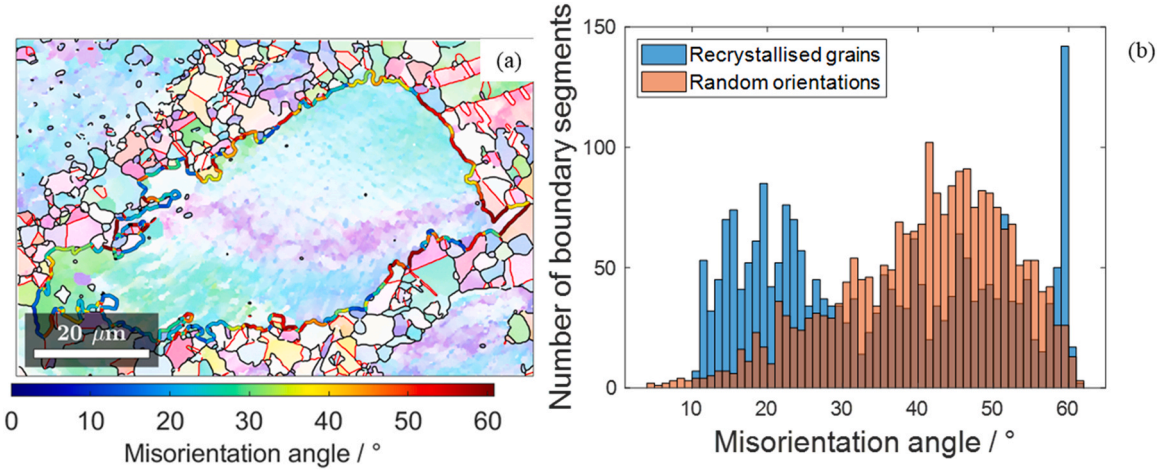

Fig. 15. Misorientation angle distribution around the initially unrecrystallized grains. (a) EBSD grain boundary map of an initially unrecrystallized grain colourised according to the local misorientation angle, (b) the distribution of misorientation angles between this grain and the surrounding recrystallized grains, shown by the blue bars. The red bars in (b) show misorientation angle distributions between the initially unrecrystallized grain and a set of random orientations in the map. Data from region 2 in Table 2 with a local strain of $\varepsilon \approx 0.72$.

Secondly, the different mechanisms affect the evolution of precipitates. The 'rectangular' precipitates in the initially statically recrystallized grains are still present after recrystallization, but the more fine and dense precipitates in the initially unrecrystallized grains are removed during recrystallization. In the initially unrecrystallized grains, sub-grains nucleate predominately at the grain boundaries. These can only grow through their boundary moving and dissolving the fine and dense precipitation encountered, leading to the removal of the fine and dense precipitation in the initially unrecrystallized grains as a consequence of recrystallization. In the statically recrystallized grains, boundaries can form around the rectangular precipitates (shown in Fig. 5). The rectangular precipitates may be partially dissolved by these boundaries, but are clearly still present after recrystallization of their host grain (as shown in Figs. 5–7). Again, the evolution of precipitates differs due to the different recrystallization mechanisms, which are themselves a consequence of microstructural heterogeneity.

These differences in recrystallization behaviour due to different precipitate distributions are qualitatively in line with the model proposed by Humphreys [28]. In this model, a sub-grain is considered to grow to a diameter D μm in a region with an orientation gradient Ω °/μm. Thus, a sub-grain is able to form a boundary with its surrounding grain which has a misorientation angle of approximately $\theta = D^*\Omega$. As such, if sub-grains are limited to below a critical size, high angle boundaries will not be able to form.

When sub-grains are of a dimension comparable to the precipitate spacing, the precipitate limited sub-grain diameter can be estimated by the spacing between the precipitates [28]. As such, regions with a smaller precipitate spacing (i.e. the initially unrecrystallized grains) will form smaller sub-grains, and recrystallized grains will be less able to form amongst the precipitates in such regions. In regions with a larger precipitate spacing (i.e. the initially statically recrystallized grains), larger sub-grains form, and recrystallized grains are more able to form amongst the precipitates in such regions.

4.4. The origin of primary γ′

The process of precipitate dissolution and reprecipitation during recrystallization calls into question the origin of primary γ′ precipitates. Primary γ′ precipitates are often thought to form at grain boundaries either during cooling from above the solvus temperature, or during solutioning (below the solvus temperature) which dissolves the other populations of γ′ [47]. The data here suggest that all precipitates in recrystallized regions of billet material are subject to dissolution and reprecipitation processes. Even the precipitates in the initially statically recrystallized grains of the as-received material, which have been shown to persist through dynamic recrystallization of their host grain, themselves form through dissolution and reprecipitation at the boundary between grains with a particular orientation relationship [26]. This implies that the primary γ′ seen in billet material (at the end of forging) is not primitive, i.e., it does not form from the first solvus crossing and persist throughout the entire forging sequence.

The primary γ′ which is undissolved during sub-solvus partial solutioning could either result from coarsening of precipitates at boundaries of the necklace recrystallized grains, or coarsening and globularisation of the "rectangular" (actually cylindrical in 3D) precipitates. In this latter case, it should be possible to find clusters of primary γ′ which share similar orientations to each other. This would require discriminating EBSD data from the γ and γ′ phases, e.g., by using coupled orientation and elemental analysis, such as EBSD-EDS or the iCHORD-SI technique [34]. The globularisation of the "rectangular" precipitates can be expected following the recrystallization of their host grain, as they will no longer share a special orientation relationship with the grains surrounding them and will thus have more isotropic interface energies, promoting globularisation during coarsening.

5. Conclusions

In this study, detailed analyses were performed on the evolution of microstructure during sub-solvus recrystallization of the recently developed AD730 Ni-based superalloy. The major observations of this work are concluded as follows:

- Within a single sample, under a single set of external TMP parameters, different local microstructures, particularly different precipitation states, lead to a range of different recrystallization mechanisms operating.
- The initially unrecrystallized grains recrystallized predominantly intergranularly, leading to relatively small recrystallized grains with little intragranular precipitation. The misorientation angle distribution of these grains with respect to their neighbouring initially unrecrystallized grain revealed a disproportionately high fraction of relatively low misorientation angles ($\lesssim 25°$) and of twin orientation relationships, implying that twinning plays an important role in the formation of dynamically recrystallized grains. This recrystallization mechanism was observed at both bulged grain boundaries, and boundaries which appeared flat (in 2D).
- Large recrystallized grains containing precipitates with an approximately twin or coherent orientation relationship, which have previously been observed to form statically, were observed to form dynamically. In 3D these precipitates have the shape of a flat cylinder.
- An intragranular recrystallization mechanism produced precipitate free recrystallized "channels" up to 75 μm long. This mechanism can produce significant grain refinement, with a "channel" of recrystallized grains splitting an initially unrecrystallized grain into two similarly orientated parts.
- Precipitates interact in at least four different ways with recrystallization:

  (i) In the necklace recrystallized grains, precipitates were dissolved into moving (sub)boundaries which they slow via solute drag, and then reprecipitated on the recrystallized side at the boundaries of recrystallized grains, generating small recrystallized grains with little intragranular precipitation.
  (ii) If a recrystallized and initially unrecrystallized grain share a < 111 > axis, precipitates can be dissolved by the recrystallization front and reprecipitated at the moving interface, with a specific orientation relationship to growing recrystallized grain.
  (iii) Precipitates can stimulate recrystallization, via the HERX mechanism.
  (iv) Large precipitates presenting a low number per unit volume may be unaffected by recrystallization, allowing continuous recrystallization processes to occur around them.

- On billet material, precipitates in recrystallized regions are the result of dissolution and reprecipitation processes associated with recrystallization. Precipitates in recrystallized regions are not "primitive", i.e., they do not persist through the entire forging process from the first solvus crossing.

CRediT authorship contribution statement

Angus Coyne: Methodology, Validation, Formal analysis, Investigation, Data curation, Writing – original draft, Visualization. **J. Blaizot:** Conceptualization, Supervision, Project administration.

S. Rahimi: Conceptualization, Supervision, Writing – review & editing. **I. Violatos:** Conceptualization, Supervision. **S. Nouveau:** Conceptualization, Supervision. **C. Dumont:** Conceptualization, Supervision. **A. Nicolaÿ:** Formal analysis, Investigation. **N. Bozzolo:** Conceptualization, Supervision, Writing – review & editing.

Declaration of Competing Interest

The authors declare that they have no known competing financial interests or personal relationships that could have appeared to influence the work reported in this paper.

Acknowledgements

The authors would like to acknowledge the support provided by Aubert & Duval, and by the Advanced Forming Research Centre (AFRC), University of Strathclyde, which receives partial funding from the UK's High Value Manufacturing CATAPULT.

References

[1] A. Devaux, B. Picque, M.F. Gervais, E. Georges, T. Poulain, P. Heritier, AD730TM - a new nickel-based superalloy for high temperature engine rotative parts, Superalloys 2012 (2012) 911–919.
[2] R.C. Reed, The Superalloys: Fundamentals and Applications, Cambridge University Press, Cambridge, 2006.
[3] F. Masoumi, M. Jahazi, D. Shahriari, J. Cormier, Coarsening and dissolution of γ′ precipitates during solution treatment of AD730TM Ni-based superalloy: mechanisms and kinetics models, J. Alloy. Compd. 658 (2016) 981–995.
[4] B.C. Xie, B.Y. Zhang, H. Yu, H. Yang, Q. Liu, Y.Q. Ning, Microstructure evolution and underlying mechanisms during the hot deformation of 718Plus superalloy, Mater. Sci. Eng. A-Struct. Mater. Prop. Microstruct. Process. 784 (2020) 11.
[5] B. Zhang, Z. Wang, H. Yu, Y. Ning, Microstructural origin and control mechanism of the mixed grain structure in Ni-based superalloys, J. Alloy. Compd. 900 (2022) 163515.
[6] A. Nicolay, G. Fiorucci, J.M. Franchet, J. Cormier, N. Bozzolo, Influence of strain rate on subsolvus dynamic and post-dynamic recrystallization kinetics of Inconel 718, Acta Mater. 174 (2019) 406–417.
[7] M. Perez, Microstructural evolution of Nimonic 80a during hot forging under non-isothermal conditions of screw press, J. Mater. Process. Technol. 252 (2018) 45–57.
[8] C. Kienl, A. Casanova, O. Messe, C. Argyrakis, C.M.F. Rae, Characterization of the Initial Stages of Dynamic Recrystallization in ATI 718Plus (R), Proceedings of the 9th International Symposium on Superalloy 718 & Derivatives: Energy, Aerospace, and Industrial Applications, 2018, pp. 405–420.
[9] D. Jia, W. Sun, D. Xu, L. Yu, X. Xin, W. Zhang, F. Qi, Abnormal dynamic recrystallization behavior of a nickel based superalloy during hot deformation, J. Alloy. Compd. 787 (2019) 196–205.
[10] T. Konkova, S. Rahimi, S. Mironov, T.N. Baker, Effect of strain level on the evolution of microstructure in a recently developed AD730 nickel based superalloy during hot forging, Mater. Charact. 139 (2018) 437–445.
[11] Y.C. Lin, X.Y. Wu, X.M. Chen, J. Chen, D.X. Wen, J.L. Zhang, L.T. Li, EBSD study of a hot deformed nickel-based superalloy, J. Alloy. Compd. 640 (2015) 101–113.
[12] S. Mitsche, C. Sommitsch, D. Huber, M. Stockinger, P. Poelt, Assessment of dynamic softening mechanisms in Allvac (R) 718PlusTM by EBSD analysis, Mater. Sci. Eng.: A 528 (10–11) (2011) 3754–3760.
[13] E. Eriksson, M.H. Colliander, Dynamic and post-dynamic recrystallization of Haynes 282 below the secondary carbide solvus, Metals 11 (1) (2021).
[14] Y. Wang, W.Z. Shao, L. Zhen, X.M. Zhang, Microstructure evolution during dynamic recrystallization of hot deformed superalloy 718, Mater. Sci. Eng. A-Struct. Mater. Prop. Microstruct. Process. 486 (1–2) (2008) 321–332.
[15] M. Azarbarmas, M. Aghaie-Khafri, J.M. Cabrera, J. Calvo, Dynamic recrystallization mechanisms and twining evolution during hot deformation of Inconel 718, Mater. Sci. Eng. A-Struct. Mater. Prop. Microstruct. Process. 678 (2016) 137–152.
[16] J.L. Qu, X.F. Xie, Z.N. Bi, J.H. Du, M.C. Zhang, Hot deformation characteristics and dynamic recrystallization mechanism of GH4730 Ni-based superalloy, J. Alloy. Compd. 785 (2019) 918–924.
[17] M.A. Charpagne, T. Billot, J.M. Franchet, N. Bozzolo, Heteroepitaxial recrystallization: a new mechanism discovered in a polycrystalline γ - γ′ nickel based superalloy, J. Alloy. Compd. 688 (2016) 685–694.
[18] S. Katnagallu, S. Vernier, M.A. Charpagne, B. Gault, N. Bozzolo, P. Kontis, Nucleation mechanism of hetero-epitaxial recrystallization in wrought nickel-based superalloys, Scr. Mater. 191 (2021) 7–11.
[19] D. Ponge, G. Gottstein, Necklace formation during dynamic recrystallization: mechanisms and impact on flow behavior, Acta Mater. 46 (1) (1998) 69–80.
[20] M.S. Chen, Y.Y. Ma, Y.C. Lin, Y.M. Lou, H.B. Li, G.Q. Wang, Q. Chen, An innovative annealing treatment method and its mechanism to refine deformed mixed grains of initial aged GH4169 superalloy, J. Alloy. Compd. 907 (2022).
[21] D.H. Liu, H.R. Chai, L. Yang, W.Q. Qiu, Z.H. Guo, Z.L. Wang, Study on the dynamic recrystallization mechanisms of GH5188 superalloy during hot compression deformation, J. Alloy. Compd. 895 (2022).
[22] J.L. Russell, M.L. Lasonde, L.A. Jackman, Microstructure development and thermal response of delta processed billet and bar for alloy 718, Superalloys 718, 625, 706 and Derivatives, Proceedings, 2005, pp. 363–372.
[23] B.J. Bond, C.M. O'Brien, J.L. Russell, J.A. Heaney, M.L. Lasonde, René 65 Billet material for forged turbine components, in: Proceedings of the 8th International Symposium on Superalloy 718 and Derivatives, 2014, pp. 107–118.
[24] C. Crozet, A. Devaux, R. Forestier, S. Charmond, M. Hueller, D. Helm, W. Buchmann, Effect of Ingot Size on microstructure and properties of the new advanced AD730TM superalloy, in: Proceedings of the 13th Intenational Symposium of Superalloys, 2016, pp. 437–446.
[25] A. Seret, C. Moussa, M. Bernacki, N. Bozzolo, On the coupling between recrystallization and precipitation following hot deformation in a γ-γ′ nickel-based superalloy, Metall. Mater. Trans. A 49A (9) (2018) 4199–4213.
[26] S. Vernier, J.M. Franchet, C. Dumont, N. Bozzolo, A. Mechanism, Leading to γ′ Precipitates with {111} facets and unusual orientation relationships to the matrix in γ–γ′ nickel-based superalloys, Metall. Mater. Trans. A 49A (9) (2018) 4308–4323.
[27] S. Vernier, J.M. Franchet, C. Dumont, P. Vennegues, N. Bozzolo, gamma' precipitates with a twin orientation relationship to their hosting grain in a gamma-gamma' nickel-based superalloy, Scr. Mater. 153 (2018) 10–13.
[28] J. Humphreys, G.S. Rohrer, A. Rollett, Recrystallization and Related Annealing Phenomena, 3rd edition., Elsevier Science Bv, Amsterdam, 2017, pp. 1–704.
[29] M. Perez, C. Dumont, O. Nodin, S. Nouveau, Impact of forging direction on the recrystallization behaviour of nickel base superalloy AD730 billet material at subsolvus temperatures, Mater. Charact. 146 (2018) 169–181.
[30] M. Pérez, C. Dumont, S. Nouveau, Gamma prime precipitate evolution during hot forging of a γ–γ′ Ni-based superalloy at subsolvus temperatures., in: S. Tin, M. Hardy, J. Clews, J. Cormier, Q. Feng, J. Marcin, C. O'Brien, A. Suzuki (Eds.) The 14th International Symposium on Superalloys (Superalloys 2021) 2020, pp. 441–449.
[31] M. Kulakov, S. Rahimi, S.L. Semiatin, Effect of deformation heating on microstructure evolution during hot forging of Ti-6Al-4V, Metall. Mater. Trans. A 53 (2) (2022) 407–419.
[32] B. El-Dasher, A. Deal, Application of electron backscatter diffraction to phase identification, in: A.J. Schwartz, M.E. Kumar, B.L.E. Adams, D.P.E. Field (Eds.), Electron Backscatter Diffraction in Materials Science, Boston, MA, 2009, pp. 81–95.
[33] M.A. Charpagne, P. Vennegues, T. Billot, J.M. Franchet, N. Bozzolo, Evidence of multimicrometric coherent γ' precipitates in a hot-forged γ-γ' nickel-based superalloy, J. Microsc. 263 (1) (2016) 106–112.
[34] S. Vernier, J.M. Franchet, M. Lesne, T. Douillard, J. Silvent, C. Langlois, N. Bozzolo, iCHORD-SI combination as an alternative to EDS-EBSD coupling for the characterization of γ-γ′ nickel-based superalloy microstructures, Mater. Charact. 142 (2018) 492–503.
[35] F. Bachmann, R. Hielscher, H. Schaeben, Grain detection from 2d and 3d EBSD data-Specification of the MTEX algorithm, Ultramicroscopy 111 (12) (2011) 1720–1733.
[36] D.G. Brandon, Structure of high-angle grain boundaries, Acta Metall. 14 (11) (1966) 1479–1484.
[37] S. Berg, D. Kutra, T. Kroeger, C.N. Straehle, B.X. Kausler, C. Haubold, M. Schiegg, J. Ales, T. Beier, M. Rudy, K. Eren, J.I. Cervantes, B.T. Xu, F. Beuttenmueller, A. Wolny, C. Zhang, U. Koethe, F.A. Hamprecht, A. Kreshuk, ilastik: interactive machine learning for (bio) image analysis, Nat. Methods 16 (12) (2019) 1226–1232.
[38] J. Schindelin, I. Arganda-Carreras, E. Frise, V. Kaynig, M. Longair, T. Pietzsch, S. Preibisch, C. Rueden, S. Saalfeld, B. Schmid, J.Y. Tinevez, D.J. White, V. Hartenstein, K. Eliceiri, P. Tomancak, A. Cardona, Fiji: an open-source platform for biological-image analysis, Nat. Methods 9 (7) (2012) 676–682.
[39] D. Legland, I. Arganda-Carreras, P. Andrey, MorphoLibJ: integrated library and plugins for mathematical morphology with ImageJ, Bioinformatics 32 (22) (2016) 3532–3534.
[40] L. Lilensten, P. Kürnsteiner, R.M. Jaber, A. Cervellon, J. Moverare, M. Segersäll, S. Antonov, P. Kontis, Segregation of solutes at dislocations: a new alloy design parameter for advanced superalloys, in: S. Tin, M. Hardy, J. Clews, J. Cormier, Q. Feng, J. Marcin, C. O'Brien, A. Suzuk (Eds.), Superalloys 2020, Seven Springs Mountain Resort, Seven Springs, Pennsylvania, USA, 2021, pp. 41–51.
[41] A. Belyakov, H. Miura, T. Sakai, Dynamic recrystallization under warm deformation of a 304 type austenitic stainless steel, Mater. Sci. Eng. A 255 (1–2) (1998) 139–147.
[42] K. Huang, R.E. Loge, A review of dynamic recrystallization phenomena in metallic materials, Mater. Des. 111 (2016) 548–574.
[43] A.M. Wusatowska-Sarnek, H. Miura, T. Sakai, Nucleation and microtexture development under dynamic recrystallization of copper, Mater. Sci. Eng. A 323 (1–2) (2002) 177–186.
[44] M. Zouari, N. Bozzolo, R.E. Loge, Mean field modelling of dynamic and post-dynamic recrystallization during hot deformation of Inconel 718 in the absence of delta phase particles, Mater. Sci. Eng. A 655 (2016) 408–424.
[45] M. Zouari, R.E. Loge, N. Bozzolo, In situ characterization of inconel 718 post-dynamic recrystallization within a scanning electron microscope, Metals 7 (11) (2017).
[46] N. Bozzolo, M. Bernacki, Viewpoint on the formation and evolution of annealing twins during thermomechanical processing of FCC Metals and Alloys, Metall. Mater. Trans. A-Phys. Metall. Mater. Sci. 51 (6) (2020) 2665–2684.
[47] M.P. Jackson, R.C. Reed, Heat treatment of UDIMET 720Li: the effect of microstructure on properties, Mater. Sci. Eng. A-Struct. Mater. Prop. Microstruct. Process. 259 (1) (1999) 85–97.